On the Shape of Dark Matter Subhalos in the Galaxy Cluster Abell 3827 and the Scattering Cross-Section of Dark Matter

Peter Taylor

Supervisors: Dr. Richard Massey and Dr. Mathilde Jauzac

A thesis presented for the degree of
Master of Science by Research

Centre for Extragalactic Astronomy
Department of Physics
Durham University
UK
November 2016

On the Shape of Dark Matter Subhalos in the Galaxy Cluster Abell 3827 and the Scattering Cross-Section of Dark Matter

Peter Taylor

Abstract

Four bright elliptical galaxies lie within the central 20 kpc of the galaxy cluster Abell 3827, indicative of an ongoing merger. Gravitational lensing has already been used to measure the offsets between dark and luminous matter. Existing measurements of an offset in one of the galaxies in this cluster suggests the presence of self-interacting dark matter (SIDM). The self-interactions scatter the dark matter (DM) particles, separating the DM halo from the collisionless stellar mass. However, offsets are not the only prediction of SIDM. Numerical simulations of some models of SIDM predict colliding halos will develop a skew in the shape of a tail. For this thesis I have developed two new parametric models to detect these tails, using gravitational lensing. These are then implemented to reconstruct the mass distribution in Abell 3827, using existing HST data, together with new integrated field spectroscopy observations from VLT/MUSE. There are three main findings. Firstly, in the new mass model of Abell 3827 there are now two galaxies where dark to luminous matter offsets are present. These offsets suggest an effective cross section for DM of $\tilde{\sigma}/m_{DM} \gtrsim 1.4$ cm^{2}g^{-1}. Secondly, the shape of the DM halo does not significantly alter the predicted offsets between the peak of the dark and luminous matter, compared to a model without skew. Finally, there are tentative signs that there may be a tail of scattered DM particles trailing one of the offset galaxies in Abell 3827.

Contents

Declaration

No part of this thesis has been submitted elsewhere for any qualification or degree. This work is based on research at the Department of Physics, Durham University, under the supervision of Dr. Richard Massey and Dr. Mathilde Jauzac.

Statment of Copyright

Acknowledgements

I would like to thank my supervisors Richard Massey and Mathilde Jauzac. I am extremely grateful for all their help and guidance throughout the year. I would also like to thank Andrew Robertson, Lydia Heck and Eric Jullo. Without them this work would not have been possible.

1 Introduction

Cosmology is incomplete. Ever since Fritz Zwicky noticed that galaxies in clusters rotate much faster than they should if the only matter present were luminous matter, astronomers have inferred the existence of a mysterious substance called Dark Matter (DM). Since then numerous lines of evidence including observations of gravitational lensing, measurements of galaxy rotation curves, and measurements of the CMB have indicated that DM is five times more prevalent by mass than ordinary matter.

The nature of DM is unknown, but it is generally assumed to be a cold collisionless particle. This thesis' primary concern is to test the second of these assertions. There are two reasons for doing this. Firstly, as there is no widely accepted particle theoretical reason for DM to be collisionless, there is no reason to assume that it is. Indeed there are many proposed models where DM has a non-negligible self-interaction cross section ([2], [3], [7], [25] and [29]). Secondly, although simulations of cold collisionless particles have done well at reproducing large scale structures in the universe, there are potentially problems at smaller scales. These include the Core vs. Cusp [9] and the Missing Satellite Problems [5]. The former is the name given to the observed under-density at the centre of dwarf galaxies and galaxy clusters compared to simulations of Cold Dark Matter (CDM). The later is the name given to the observed under-abundance of satellite galaxies in the local group. It was first proposed in [42] that SIDM could solve both of these problems, by scattering DM particles out of over-dense regions. However, SIDM is not the only explanation for these discrepancies ([37], [39] and [43]).

While SIDM may not be unique in solving these problems, some models of SIDM also predict an offset between dark and luminous matter in colliding halos caused by the scattering of DM particles . This separates the largely collisionless stellar component from the rest of the dark matter halo, overcoming the attractive gravitational force between the two components. In certain collisional systems it is possible to reconstruct the mass distribution using gravitational lensing, and by measuring such offsets, to constrain the cross-section of dark matter, σ/m.

This method has been used to compute numerous upper bounds for the momentum transfer self-interaction cross-section, a measure of how much momentum is transferred per unit of mass. This analysis was first done in [33], on the Bullet Cluster, which is a pair of merging galaxy clusters. This study found an upper bound on the cross section of $\sigma/m < 5$ cm ^{2} g $^{-1}$. More recently by measuring the offsets between luminous and dark matter in 30 clusters, [15] placed an upper bound on the self-interaction cross-section of $\sigma/m < 0.47$ cm ^{2} g $^{-1}$. More recently, by measuring offsets in an individual cluster, Abell 2744, [18] found an upper bound of $\sigma/m < 1.28$ cm ^{2} g $^{-1}$.

More interestingly however, a 3σ-level offset measurement of approximately 1.5 kpc between the luminous and dark matter mass peak, in a central elliptical galaxy, in the galaxy cluster Abell 3827, was made in [34] and used to place a lower bound on the self-interaction cross section of DM: $\sigma/m > 2$ cm ^{2} g $^{-1}$, as computed in [23]. A similar offset has been measured in [41], in a pair of field galaxies. The authors noted that there are still a large number of unanalysed field galaxy lensing pairs found in the SLACS survey, so the number of measured offsets could greatly increase.

It is still too early to tell if these offset measurements are the first observed effects of SIDM. The primary difficulties are: isolating the effects of SIDM from less exotic physics like gas effects, tidal forces and dynamical friction; and producing mass maps with the required accuracy from gravitational lensing.

In [40] no offsets were found in a large ΛCDM N-body simulation. This suggests that offsets are not the result of less exotic physics. However, simulations conducted in [38], of the Bullet Cluster, indicate that shocked gas, which is gravitationally coupled to the DM halo, could lead to similar offsets. This should not be a large issue for the offsets measured in Abell 3827, since the gas fraction of central ellipticals is low, but this could pose more of a challenge for the SIDM interpretation of offsets in field galaxies. The simulations in [22], [27] and [38] also predict two additional effects for colliding SIDM halos. The first, is that particles being scattered out of the halo will create a skewed distribution in the shape of a tail, trailing the direction of motion. The second effect, irrespective of the presence of SIDM, is due to tidal forces, which will distort the shape of colliding DM halos to form a tail in the opposite direction, so that the tails of the two galaxies point towards each other. This is somewhat unexpected behaviour, so the reason for this will be explained in Section 3.1.

The primary aim of this work is to determine whether DM tails are present using gravitational lensing. Section 3 covers relevant background material in gravitational lensing and particle physics. In Section 4 skewed halos are discussed, and a new skewed parametric density profile is introduced to detect DM tails. Existing mass models and new data for the collisional cluster Abell 3827 are discussed in Section 5. New lens modelling for this cluster is presented in Section 6. This includes the use of the new skewed parametric halo. The physical interpretation of the resulting mass model is discussed in Section 7. Finally I discuss directions for further work in section 8. The appendix contains a brief discussion about the validity of the assumptions made in gravitational lensing, as well as another parametric model for a skewed lens, and a lens where the ellipticity varies as a function of radius.

Throughout I assume a cosmology with $\Omega_M = 0.3$, $\Omega_\Lambda = 0.7$ and $H_0 = 70$ km s^{-1} Mpc^{-1}, so that at the redshift of Abell 3827, z= 0.99, $1''$ corresponds to 1.828 kpc.

2 Background

In this section I aim to provide a concise overview of the theoretical underpinnings of this thesis. This covers gravitational lensing and its formalism, followed by a discussion of the link between offset measurements and the particle theoretic nature of DM.

2.1 Gravitational Lensing Overview

Einstein's General Theory of Relativity (GR) has been a resounding success predicting the precession of the perihelion of Mercury, gravitational time delays, and the deflection of light by (large) gravitational potentials.

The last of these phenomena is referred to as gravitational lensing. It is caused as massive bodies distort space-time and photons travel along geodesics ("the shortest path between two points").

There are two gravitational lensing regimes: strong and weak. In the former, multiple photons from the same source head off in different directions. An intermediate mass deflector bends the light so that the same source appears as multiple images, as viewed from Earth. The positions of these multiple sources can then be used to reconstruct the mass distribution of the deflector. For a review of strong lensing by galaxy clusters, see [28]. In contrast, in the weak lensing regime, the shapes of galaxies are slightly distorted. This distortion can be written in terms of two scalars, called the convergence and shear, which determine the isotropic and anisotropic local distortion, respectively. The former is proportional to the deflector mass density. For a large sample of background galaxies, the average ellipticity is a good approximation for the shear. Once the shear is known, the convergence, and hence the deflector mass density, can be computed. See [24] for more details. For a review of weak gravitational lensing see [1].

The work presented in this thesis reconstructs the lens mass distribution using strong gravitational lensing exclusively. Strong lensing reconstruction methods fall into two categories: non-parametric and parametric.

Non-parametric methods make no assumptions about the underlying mass distribution of the lens. An initial seed mass is iteratively perturbed on an adaptive grid to find the mass distribution that best reproduces the position of the observed images. This process may be repeated many times, and then averaged over. For more details on how this is done in practice see [11], [30] and [21].

In contrast many parametric lensing techniques assign parametric DM halos to the galaxy cluster, and to some of the visible galaxies. Each halo is given a number of free parameters which are estimated using Markov Chain Monte Carlo (MCMC) methods. More details can be found in [20]. For a comparison between their performance in simulated galaxy clusters see [35]. Although there are merits to the non-parametric approach, (for example non-parametric lensing can test the light-traces-mass hypothesis in galaxy clusters), I will use the parametric approach. Using parametric methods, with appropriately defined parameters, will make it possible to directly measure the skew of a DM halo.

2.2 Gravitational Lensing Formalism

All of gravitational lensing boils down to computing the deflection angle, as shown in Figure 1, for a photon in a static space-time. This is derived in [8], and is given by

$$\hat{\alpha} = \frac{2}{c^2} \int \nabla_{\perp} \Phi \, \mathrm{d}s, \tag{1}$$

where Φ is the gravitational potential of the lens, $\mathrm{d}s$ is the physical distance element and the perpendicular gradient, $\nabla_{\perp}$, is defined as the difference between the total gradient and the gradient along the path travelled.

To find the deflection angle due to a point mass, orient the axis system so that if the mass was not there the photon would travel along the x-axis, and let $\mathbf{b}$ be the vector pointing from the point mass to the point of nearest approach on the perturbed path. Now,

$$\Phi = -\frac{GM}{r} = -\frac{GM}{(b^2 + x^2)}. \tag{2}$$

This implies:

$$\nabla_{\perp} \Phi = \frac{GM}{(b^2 + x^2)^{3/2}} \boldsymbol{b}. \tag{3}$$

It then follows from equation (1) that the deflection angle is:

$$\begin{aligned} \hat{\alpha} =& \frac{2GMb}{c^2} \int_{-\infty}^{\infty} \frac{\mathrm{d}x}{(b^2 + x^2)^{3/2}} \\ =& \frac{4GM}{c^2 b}. \end{aligned} \tag{4}$$

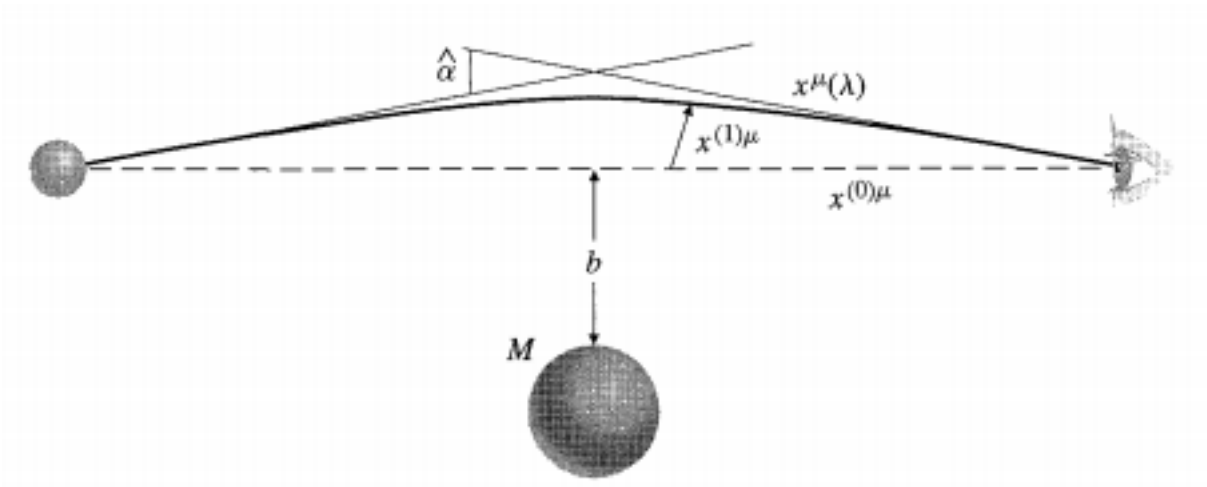

Figure 1: Here the source on the left is being gravitationally lensed by a mass M with impact parameter b. The deflection angle is $\hat{\alpha}$. The path $x^{(0)\mu}$ is the path the photon would follow if no mass were present between the observer and the source, and $x^{(1)\mu}$ is the first order perturbation due to the gravitational deflection caused by M. This figure is reproduced from [8]

.

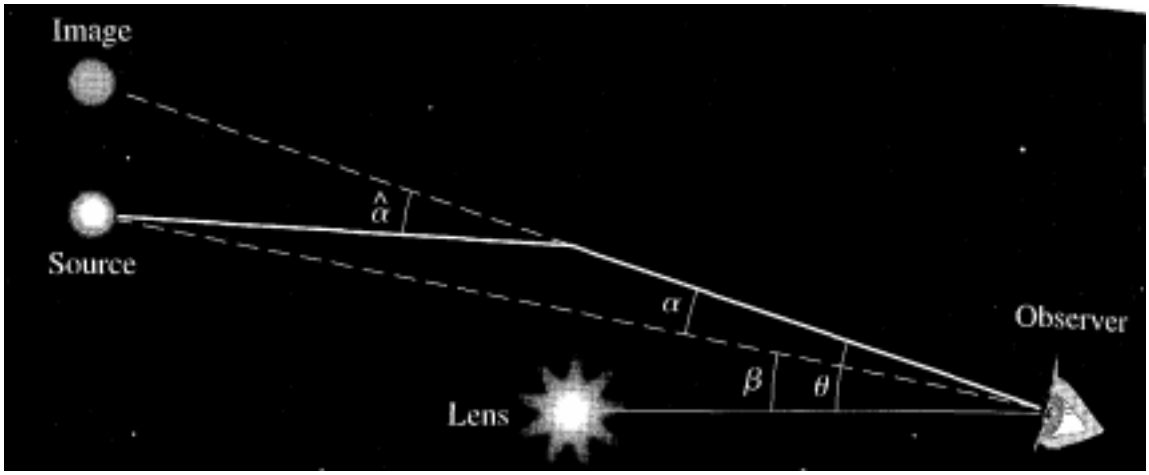

Figure 2: This figure shows the relationship between $\hat{\alpha}$ and α. It is adapted from [8]

As is the case in classical optics, the deflection angle as perceived by an observer is dependent on the distances to the lens and the lensed source. It can be shown that the deflection angle from the observer's perspective, as shown in Figure 2, is given by

$$\alpha = \frac{D_{ls}}{D_s}\hat{\alpha}, \tag{5}$$

and $b = D_l\theta$ where θ is the angle on the sky and D_{ls}, D_s and D_l are the angular diameter distances from the lens to the source, the observer to the source, and the observer to the lens respectively. We now make the Thin Lens Approximation and project all the mass for an object onto a plane. This approximation is valid as long as the size of the object is small compared to the distance to the observer. The validity of this assumption is tested in the Appendix. Integrating over the two dimensional projected mass density $\Sigma(\boldsymbol{\theta'})$ gives:

$$\boldsymbol{\alpha}(\boldsymbol{\theta}) = \frac{4G}{c^2}\frac{D_l D_{ls}}{D_s}\int \Sigma(\boldsymbol{\theta'})\frac{\boldsymbol{\theta}-\boldsymbol{\theta'}}{|\boldsymbol{\theta}-\boldsymbol{\theta'}|^2}\mathrm{d}^2\boldsymbol{\theta'} \tag{6}$$

It is in general very difficult to integrate this analytically, for a given density. The form of this expression is very similar to the formula giving the force due to an arbitrary mass distribution in Newtonian Gravity. Inspired by this, and to make calculations simpler, it is possible to define a projected gravitational potential, $\psi(\boldsymbol{\theta})$, which solves the Poisson Equation:

$$\Sigma(\boldsymbol{\theta}) = \frac{c^2}{8\pi G}\frac{D_s}{D_l D_{ls}}\nabla^2_{\boldsymbol{\theta}}\psi(\boldsymbol{\theta}). \tag{7}$$

with $\psi \to \infty$ as $\theta \to \infty$, so that

$$\boldsymbol{\alpha}(\boldsymbol{\theta}) = \nabla_{\boldsymbol{\theta}}\psi(\boldsymbol{\theta}). \tag{8}$$

In terms of the density, this potential is given by:

$$\psi(\boldsymbol{\theta}) = \frac{4G}{c^2}\frac{D_l D_{ls}}{D_s}\int \Sigma(\boldsymbol{\theta'})\log|\boldsymbol{\theta}-\boldsymbol{\theta'}|\,\mathrm{d}^2\boldsymbol{\theta'}. \tag{9}$$

Before moving on, it is also worth mentioning three other lensing phenomena. As photons from an object are deflected by slightly different angles, a gravitational lens will

magnify a background image and by Liouville's Theorem which implies the conservation of photon density in phase space, conserve surface brightness. The magnification is given by

$$\mu = \frac{1}{\det A}, \tag{10}$$

where:

$$A_{ij} \equiv \delta_{ij} - \partial_{x_i}\partial_{x_j}\psi. \tag{11}$$

and δ_{ij} is the Kronecker Delta function.

Secondly, if a source lies directly behind a circularly symmetric lens, the source will be lensed into a circle. The radius of this circle, called the Einstein Radius, is given by:

$$R_E = \sqrt{\frac{4GM}{c^2}\frac{D_l D_{ls}}{D_s}}. \tag{12}$$

Finally, in the Thin Lens Approximation, there will always be an odd number of multiple images [6]. These effects will be noted when modelling Abell 3827.

2.3 The Link to Particle Physics

A calculation presented in [22] is shown in this section, and then modified to more accurately model the gravitational restoring force between offset components. The ultimate purpose of this, is to measure the cross-section of DM. This is a quantity that is independent of the exact type of scattering processes, depending only on the mass of the particle, the momentum exchanged in each collision, the collision velocity, and the distribution of DM in galaxies. This allows a comparison between different models of SIDM. Similar computations have been performed in [16] and [44], however the one presented here is preferable as the link to particle physics is more apparent.

In [22] two halos containing SIDM are colliding. For simplicity we assume the DM particles in galaxy 1 move at a constant velocity v_0, and galaxy 2 is at rest. The density of DM in galaxy 2 is denoted ρ_2, and the mass of a DM particle is denoted m_{DM}.

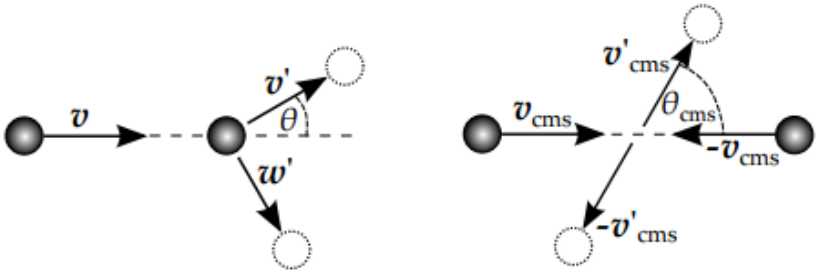

Figure 3: A scattering process involving two SIDM particles. On the left hand side a particles in galaxy 1 collides with a particle at rest in galaxy 2 with velocity v. The right hand side shows the same scattering process in the centre of mass frame. This figure is taken from [22].

Suppose now that a scattering event occurs between two SIDM particles, one from galaxy 1 and the other from galaxy 2. As in Figure 3. In the centre of mass frame, the velocity parallel to the collision is:

$$\delta v_{par} = v_0 \left(1 - \cos\left(\theta_{cms}\right)\right). \tag{13}$$

By symmetry the change in velocity in the perpendicular direction can be ignored, by averaging over a large number of collisions. The number of collisions in time $\mathrm{d}t$ is:

$$\begin{aligned}\mathrm{d}C &= \text{Number of particles} \times \text{Velocity} \times \text{Time} \times \text{Area} \\ &= \left(\frac{\rho_2}{m_{DM}}\right) \times v_0 \times \mathrm{d}t \times \left(\frac{\mathrm{d}\sigma}{\mathrm{d}\Omega_{cms}}\mathrm{d}\Omega_{cms}\right),\end{aligned} \tag{14}$$

where the differential cross-cross section, $\frac{\mathrm{d}\sigma}{\mathrm{d}\Omega_{cms}}$, measures the probability of the particle being scattered inside the differential solid angle, $\mathrm{d}\Omega_{cms} = \mathrm{dcos}\theta_{cms}\mathrm{d}\phi_{cms}$. Hence, the deceleration of galaxy 1 due to collisions is given by:

$$\begin{aligned}\mathrm{a} =& \int \delta v_{par} \frac{\mathrm{d}C}{\mathrm{d}t}\mathrm{d}t \\ =& \frac{\rho_2 v_0^2}{m_{DM}} \int \left(1 - \cos\left(\theta_{cms}\right)\right) \frac{\mathrm{d}\sigma}{\mathrm{d}\Omega_{cms}}\mathrm{d}\Omega_{cms} \\ =& \frac{\rho_2 v_0^2 \sigma_T}{2m_{DM}},\end{aligned} \tag{15}$$

where the *momentum transfer cross section* is defined as

$$\sigma_T \equiv 4\pi \int_0^1 \mathrm{dcos}\theta_{cms} \left(1 - \cos\left(\theta_{cms}\right)\right) \frac{\mathrm{d}\sigma}{\mathrm{d}\Omega_{cms}}. \tag{16}$$

This looks like the normal formula for a cross-section, weighted by a factor of $1 - \cos\left(\theta_{cms}\right)$, which accounts for the difference between the relative velocity parallel to the direction of initial motion before and after the collision. Thus the momentum transfer cross-section is a measure of the amount of momentum exchanged during scattering.

It is important to note that this is different from the usual definition of the momentum transfer cross-section where the integral is evaluated in the range $[-1, 1]$. This is to take into account the fact that because dark matter particles are indistinguishable, if $\theta_{cm} > \pi/2$, the particles can be relabelled in such a way that $\theta_{cm} < \pi/2$, as if no collision took place.

For isotropic scattering we see that this definition of σ_T gives, $\sigma = 2\sigma_T$, where σ is the usual cross-section. This motivates the definition of the *effective cross section*

$$\tilde{\sigma} \equiv 2\sigma_T. \tag{17}$$

Equations (15) and (17) then lead to an equation for the effective drag force:

$$\frac{F_{drag}}{m_{DM}} = \frac{\rho_2 v_0^2}{4} \frac{\tilde{\sigma}}{m_{DM}}. \tag{18}$$

Now to make the link with astrophysics, following analysis given in [23], assume that the drag force can be modelled by equation (18). For an offset to occur it must be the case that:

$$\frac{F_{drag}}{m_{DM}} > \frac{F_{sh}}{m_{\mathrm{star}}}, \tag{19}$$

where F_{sh} is the gravitational force between the stars and the DM subhalo. Now

$$\frac{F_{sh}}{m_{star}} = \frac{GM_{sh}\left(\Delta\right)}{\Delta^2}, \tag{20}$$

where Δ is the separation between the subhalo and stars and $M_{sh}(\Delta)$ is the mass of the stellar halo within a radius Δ. For this estimate a constant density core is assumed so that:

$$M_{sh}(\Delta) = M_{sh}\frac{\Delta^3}{a_{sh}^3}, \tag{21}$$

where a_{sh} is the scale radius of the core. Equations (20) and (21) together imply that the gravitational restoring force is proportional to the offset, Δ. For small separations this is the same behaviour that is found in [16], where the authors perform a more complete analysis computing the returning force between two extended overlapping halos. Substituting equations (18) and (20) into (19) gives:

$$\frac{\tilde{\sigma}}{m_{DM}} > \frac{4}{v_0^2\rho_2}\frac{GM_{sh}(\Delta)}{\Delta^2}. \tag{22}$$

In the case of Abell 3827, the authors estimate $a_{sh} = 2.7$ kpc, $M_{sh} = 7\times10^{10}M_{\odot}$, $\Delta = 1.6$ kpc, $\rho = 4$ Gev cm $^{-3}$ and $v = 1500$ km s^{-1}. These values are all taken from [34], or are reasonable values for a halo found at this distance from the centre of a galaxy cluster. This yields:

$$\frac{\sigma}{m_{DM}} \gtrsim 2 \text{ cm}^2 \text{ g}^{-1}. \tag{23}$$

This is a very rough calculation, and fails to treat the gravitational restoring force correctly, which, in reality, is between two overlapping extended halos. To calculate this correctly, consider a coordinate system where the centre of the DM halo lies at the origin, and the centre of the stellar mass lies along the positive x-axis at a separation S, with coordinate $\boldsymbol{S}$. Now consider an infinitesimal mass element of dark matter at a coordinate $\mathbf{r}_D$, with mass $\rho_D(\mathbf{r}_D)\,\mathrm{d}^3\mathbf{r}_D$. The magnitude of the restoring force on this element is given by:

$$\frac{\mathrm{d}F_{sh}}{m_{stars}} = -\frac{G}{m_{stars}}\frac{M_s(|\mathbf{r}_D - \mathbf{S}|)\,\rho_D(\mathbf{r}_D)\,\mathrm{d}^3\mathbf{r}_D}{|\mathbf{r}_D|^2}, \tag{24}$$

where $M_s(|\mathbf{r}_D - \mathbf{S}|)$ gives the stellar mass enclosed inside the radius between the stellar mass peak and mass element, centred about the stellar mass peak. Here we are assuming that the stellar mass distribution is spherically symmetric and have made use of this by applying Newton's Shell Theorem, centred about the stellar mass peak. Hence, the total restoring force in the offset direction is:

$$\frac{F_{sh}}{m_{stars}} = -\frac{4G}{m_{stars}}\int_{y>0,\ z>0}\frac{M_s(|\mathbf{r}_D - \mathbf{S}|)\,\rho_D(\mathbf{r}_D)}{|\mathbf{r}_D|^3}\mathbf{r}_D\cdot\mathbf{e}_x\ \mathrm{d}^3\mathbf{r}_D, \tag{25}$$

where $\mathbf{e}_x$ is the unit vector in the x-direction, and we have used symmetry about $x = 0$ and $y = 0$. I model the stellar distribution using a Hernquist profile [17]. For this profile, the mass enclosed inside a radius r, $M(r)$, is given by:

$$M(r) = M\frac{r^2}{r^2 + a^2}, \tag{26}$$

where M is the total mass, and a is the scale radius. I model the DM component using a Pseudo Isothermal Elliptical Mass Distribution (PIEMD). Details can be found in [32]. In particular, on taking the limit as $r_{cut}\to\infty$, the density profile is given by:

$$\rho_D(r) = \frac{\rho_0}{1 + (r/r_{core})^2}, \tag{27}$$

where

$$\rho_0 = \frac{\sigma_0^2}{2\pi G}\frac{1}{r_{core}^2}. \tag{28}$$

Plugging equations (26) and (27) into equation (25) gives :

$$\frac{F_{sh}}{m_{stars}} = -\frac{2\sigma_0^2}{\pi}\frac{1}{r_{core}^2} I\left(S\right), \tag{29}$$

where I is given by:

$$I\left(S\right) \equiv \int_{y>0,\ z>0} \frac{|\mathbf{r}_D - \mathbf{S}|^2}{\left(|\mathbf{r}_D - \mathbf{S}| + a_{stars}\right)^2} \frac{1}{\left(1 + \left(r/r_{core}\right)^2\right)} \frac{x}{|\mathbf{r}_D|^3}\ \mathrm{d}^3\mathbf{r}_D. \tag{30}$$

Plugging (29) into (19) and using (18) gives:

$$\frac{\tilde{\sigma}}{m_{DM}} > -\frac{8\sigma_0^2}{\pi}\frac{1}{r_{core}^2\rho_2 v_0^2} I\left(S\right). \tag{31}$$

I will show later that modelling the restoring force in this way leads to only a small difference in the estimated cross-section.

There are, of course, many other types of potential scattering processes: including velocity dependent scattering and mediator particle scattering which may have very different behaviours [22]. More simulations, and more offset measurements, will hopefully continue to narrow the parameter space of allowed scattering processes and cross-sections.

3 Skewed Lenses

In this section I discuss the need for a parametric model describing a skewed gravitational lens. I show how this can be done using a coordinate transformation approach. Finally the deflection angle for this new parametric lens is computed analytically. Another approach for introducing skew is discussed in the Appendix.

3.1 The Need For Skew

Offsets are not the only prediction of SIDM. Simulations conducted in [22] found that as SIDM particles are scattered out of colliding halos, the halos will develop a skew in the shape of a tail. This can be seen in Figure 4.

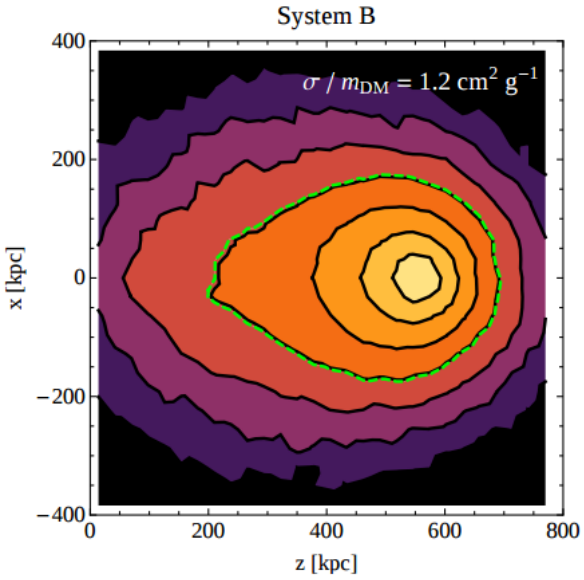

Figure 4: The apparently skewed projected surface mass density of SIDM in a simulation of the Bullet Cluster, performed in [22]. This halo has already passed through another halo and is moving from left to right in this figure. The skewed tail on the left is caused by DM particles that have been scattered out of the potential well. As this is a simulation of colliding clusters, the characteristic length scale is much larger than it would be for colliding galactic halos.

If SIDM is present, the direction of the tail will indicate the collision direction. The presence of a tail also indicates the form of scattering SIDM undergoes. A small momentum transfer scattering process, occurring frequently, would not transfer enough energy to scatter DM particles out of the halo. In this scenario a merging halo would retain elliptical symmetry as the collisions act as an effective drag force slowing down the halo [22]. On the other hand, an infrequent high momentum transfer scattering would lead to particles escaping the halos' potential well, leading to a tail of trailing DM particles [22].

It was also found in [38] that tidal forces in colliding halos could distort the shape of the gravitational lens away from elliptical symmetry. Fitting a mass model in which the contours of equal density are concentric ellipses, in the lensing reconstruction, to halos that are in reality skewed could lead to false detections of offsets.

3.2 Tidal Forces and Skewed Lenses

As discussed above, tidal forces can lead to non-elliptically symmetric halos. This is unexpected as the Moon deforms the Earth symmetrically into an ellipsoid. Should this not be the same for DM halos? No it is not, because the relative size of the Earth to the distance to the Moon is small, whereas the size of colliding DM halo compared to the distance to its nearest companion is large.

To see why this scale comparison is relevant, I will follow an argument originally given by Andrew Robertson. Consider three test masses, each with mass m, lying inside a DM halo near a "point mass" halo of mass M, at a distances: r, $r - \mathrm{d}r$ and $r + \mathrm{d}r$. The difference in forces between the first and last of these masses is:

$$\begin{aligned}
\nabla F =& \frac{GMm}{(r+\mathrm{d}r)^2} - \frac{GMm}{r^2} \\
=& \frac{GMm}{r^2}\left(\frac{1}{\left(1+\frac{\mathrm{d}r}{r}\right)^2} - 1\right) \\
=& \frac{GMm}{r^2}\left(-\frac{2\mathrm{d}r}{r} + O\left(\mathrm{d}r^2\right)\right) \\
=& -\frac{2GMm}{r^3}\mathrm{d}r + O\left(\mathrm{d}r^2\right).
\end{aligned}$$

The point is, when $\mathrm{d}r \ll r$, like in the Earth-Moon system, we can ignore all the higher order terms. This means that the difference in forces are anti-symmetric about the mass at r, because the difference in forces between r and $r - \mathrm{d}r$ is given by:

$$\nabla F = \frac{2GMm}{r^3}\mathrm{d}r + O\left(\mathrm{d}r^2\right).$$

However, if it is not the case that $\mathrm{d}r \ll r$, then the second order term can no longer be neglected. The second order term has a positive sign in both cases, so that the difference in forces for the mass at $r - \mathrm{d}r$ and $r + \mathrm{d}r$ is no longer anti-symmetric about r.

In simulations this lack of symmetry is responsible for two effects [38]. Firstly, two colliding halos will develop tails pointing towards each other. Secondly the peak of the projected mass densities will be pulled towards one another relative to the exterior isodensity contours. (See top panel of Figure 5). Since the effect of tidal forces will partially cancel those caused by SIDM scattering, any skewness measured is likely to be an underestimate of the skewness caused by SIDM scattering.

3.3 Lenstool and the Pseudo Isothermal Elliptical Mass Distributions

Lenstool is a publicly available parametric Bayesian Markov-Chain Monte Carlo (MCMC) mass reconstruction package [20]. By combining a cluster scale halo together with galactic scale halos, each with a number of free parameters, Lenstool explores the parameter space to find the mass distribution that best reproduces the positions of the multiply-lensed images, and computes the posterior distribution for all free parameters.

Lenstool has a number of different lens profile options, which until now have all been elliptically symmetric. In this thesis, I modify the Pseudo Isothermal Elliptical Mass Distribution (PIEMD) profile originally introduced in [26]. The PIEMD is appealing as it is possible to analytically integrate it to compute deflection angles. This allows the MCMC computation to be done quickly.

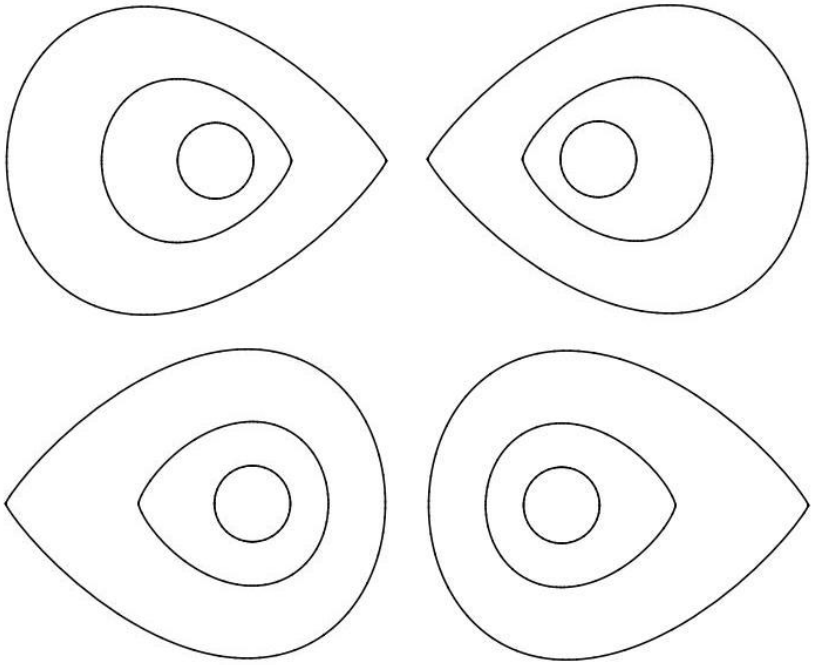

Figure 5: The top and bottom panel show an exaggerated schematic of the skewed isodensity contours for two merging halos, before they have passed through one another, in two different scenarios. In the top panel tidal forces dominate, causing tails pointing towards the centre of the collision and a peak that has moved towards the centre. In the bottom panel SIDM scattering dominates the formation skew, causing a tail of trailing scattered DM particles.

The surface mass density of the PIEMD, used in Lenstool, is:

$$\mathbf{\Sigma}(\mathbf{r}) \equiv \frac{r_{\rm cut} - r_{\rm core}}{r_{\rm cut} r_{\rm core}} \left(\frac{\rho_0}{\sqrt{r_{\rm cut}^2 + r_{em}^2}} - \frac{\rho_0}{\sqrt{r_{\rm core}^2 + r_{em}^2}} \right), \tag{32}$$

where ρ_0 is proportional to the square of velocity dispersion σ_0^2. The elliptical radius, in the notation of [26], is given by:

$$r_{em} \equiv \sqrt{\frac{x^2}{1+\epsilon^2} + \frac{y^2}{1-\epsilon^2}}, \tag{33}$$

where the ellipticity of the halo, $\epsilon \equiv \frac{u-v}{u+v}$, and u and v give the major and minor axis respectively.

This can be integrated, using methods from complex analysis, as in [26], to find the lensing potential and deflection angle. In particular the lensing potential is given by:

$$\psi(\mathbf{r}) \equiv \frac{as}{s-a} \left(a^{-1}\psi_a - s^{-1}\psi_s \right) \tag{34}$$

where s is the cut radius, and a is the core radius, so that the cut and core potentials are given by:

$$\psi_\omega(\mathbf{r}) \equiv \frac{E_0 \omega (1-\epsilon^2)}{2 r_{em} \sqrt{\epsilon}} \ \text{Im} \ \left[(x - iy) K^\star \right], \tag{35}$$

with $\omega \in \{a, s\}$, where,

$$E_0 \equiv 6\pi \frac{D_{ls}}{D_s} \frac{v_{\sigma_0^2}}{c^2}, \tag{36}$$

and,

$$\begin{aligned} K^\star \equiv & \sinh(2\eta) \log\left[\frac{\cosh^2\eta}{\cosh(\eta+\zeta)\cosh(\eta-\zeta)}\right] \\ & + \sinh(2\zeta) \log\left[\frac{\cosh(\eta+\zeta)}{\cosh(\eta-\zeta)}\right], \end{aligned} \tag{37}$$

$$\zeta \equiv \frac{1}{2} \log\left(\frac{r_{em} + \sqrt{r_{em}^2 + \omega^2}}{\omega}\right), \tag{38}$$

and

$$\eta \equiv \frac{1}{2} \sinh^{-1}\left(\frac{2\sqrt{\epsilon}}{1-\epsilon} \sin\chi\right) + \frac{i}{2} \sin^{-1}\left(\frac{2\sqrt{\epsilon}}{1+\epsilon} \cos\chi\right), \tag{39}$$

with $x = r\cos\chi$ and $y = r\sin\chi$. Using equation 8, the deflection angles can be computed from the first derivatives, which are given by:

$$\frac{\partial\psi}{\partial x} + i\frac{\partial\psi}{\partial y} = \frac{(1-\epsilon^2)E_0}{2i\sqrt{\epsilon}} \log \frac{\left[\frac{1-\epsilon}{1+\epsilon}x - i\frac{1+\epsilon}{1-\epsilon}y + 2i\sqrt{\epsilon}\sqrt{\omega^2 + \frac{x^2}{(1+\epsilon)^2} + \frac{y^2}{(1-\epsilon)^2}}\right]}{(x - iy + 2i\omega\sqrt{\epsilon})}. \tag{40}$$

One caveat worth mentioning is that the theoretical velocity dispersion used above, $\sigma_{0_{th}}^2$, is not the same as the velocity dispersion output by Lenstool, $\sigma_{0_{lt}}^2$. They are related by the relation:

$$\sigma_{0_{th}}^2 = \frac{2}{3}\sigma_{0_{lt}}^2. \tag{41}$$

For more details see: *https://projets.lam.fr/projects/lenstool/wiki/PIEMD* .

3.4 Coordinate Transformation Approach

For a skewed lens model to be computationally efficient in Lenstool, an analytic expression for the deflection angle at each point in the lens plane is necessary. It is in general very difficult to get an analytic expression for the deflection angle in terms of the mass density, given by integrating equation 6. Such a computation can be done for a PIEMD using methods from complex analysis introduced in [4], but this will not work for a skewed lens, as these methods rely on elliptical symmetry.

To introduce the skew, we will start with an elliptically symmetric mass distribution and make a coordinate transformation that maps concentric circles centred about the origin, to ellipses with a shared focus at the origin. It is highly non-trivial to apply the coordinate transformation to the mass distribution, as we would then have to integrate up to find the deflection angles. Instead I will apply the coordinate transformation to the lensing potential and differentiate down to compute the deflection angles and mass distributions, using equations (8) and (7) respectively. In particular, the lensing potential, ψ, is transformed so that:

$$\psi(x, y) \to \psi'(x, y) \equiv \psi(x', y'). \tag{42}$$

The first and second derivatives can then be computed analytically with applications of the chain rule. For example, the first x-derivative of the potential is given by:

$$\psi'_x = \left(\psi_{x'}(x', y')\, x'_x + \psi_{y'}(x', y')\, y'_x\right)\big|_{(x,y)}, \tag{43}$$

where the subscript denotes partial differentiation.

To find the appropriate coordinate transformation, note the equation of an ellipse with a focus at the origin is given by:

$$r(\theta) = \frac{a(1-e^2)}{1+e\,\cos(\theta)}, \tag{44}$$

where a is the semi-major axis and e is the ellipticity defined by:

$$e \equiv \sqrt{1-(b/a)^2}\,. \tag{45}$$

Thus we require a transformation such that:

$$r \to r' \equiv \frac{r(1-e^2)}{1+e\,\cos(\theta)}. \tag{46}$$

Hence we make the transformation:

$$\begin{aligned} x \to x' &\equiv \frac{r(1-s^2)}{1+s\,\cos(\theta-\phi_s)}\,\cos(\theta) \\ y \to y' &\equiv \frac{r(1-s^2)}{1+s\,\cos(\theta-\phi_s)}\,\sin(\theta)\,, \end{aligned} \tag{47}$$

where we have replaced the eillipticity, e, with the skew, s, and θ with $\theta-\phi_s$, which sets the skew angle. A slight modification is actually implemented so that we instead take:

$$\begin{aligned} x \to x' &\equiv \frac{r(1-s^2)^{3/4}}{1+s\,\cos(\theta-\phi_s)}\,\cos(\theta) \\ y \to y' &\equiv \frac{r(1-s^2)^{3/4}}{1+s\,\cos(\theta-\phi_s)}\,\sin(\theta)\,. \end{aligned} \tag{48}$$

For the remainder of this thesis, all skew angles will be given in radians. The domain is restricted to $|s| \in [0,1)$, and ϕ_s lies in some interval of length π. This ensures that the parameter space is explored symmetrically about $s=0$, so that Lenstool can recover $s=0$, when no skew is present.

3.5 The Pseudo Isothermal Skewed Potential

We apply the coordinate transformation, given in the previous section, to the PIEMD potential. This will be referred to as the Pseudo Isothermal Skewed Potential (PISP). The resulting isodensity contours are shown in Figure 6.

For large skews the PISP encounters problems, as we had to make the coordinate transformation to the potential, and not the mass density. In particular, large skew values can act to completely overwhelm the underlying ellipticity. This can be seen in Figure 7. This makes it difficult to isolate the effects of skew and ellipticity, for large skews. For this reason I will set the prior boundaries small enough to ensure that this does not happen.

It is not the case that a PISP will have the same mass as a PIEMD with the same underlying parameters, excluding skew. However, I have checked a wide variety of different circumstances, and the peak of the projected density for a PISP and a PIEMD lie at

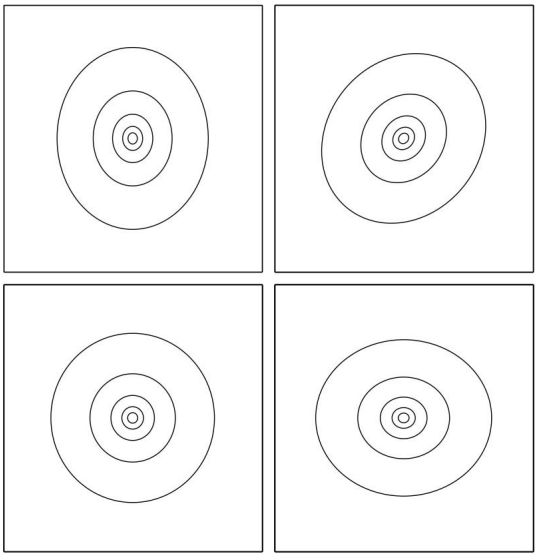

(a) PIEMD in 20×20 kpc box.

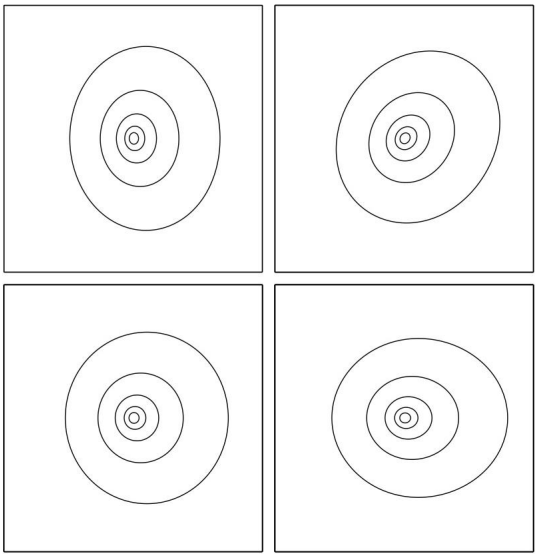

(b) PISP with small skew to the right.

Figure 6: The right hand side shows the isodensity contours of four PISP contours. The left hand side shows these same density profiles with no skew. In all cases the cut radius is fixed to 73.1 kpc, the core radius is fixed to 0.183 kpc and the velocity dispersion is 180 km s^{-1}. The ellipticity is 0.15 for the three galaxies starting at the top left and going clockwise with orientations of $90°, 45°$ and $0°$ respectively. The halos in the bottom left hand corners have ellipticities of $0°$. The skew acts to the right, $\phi_s = \pi/2$, where it is present, with the skew parameter, $s = 0.15$.

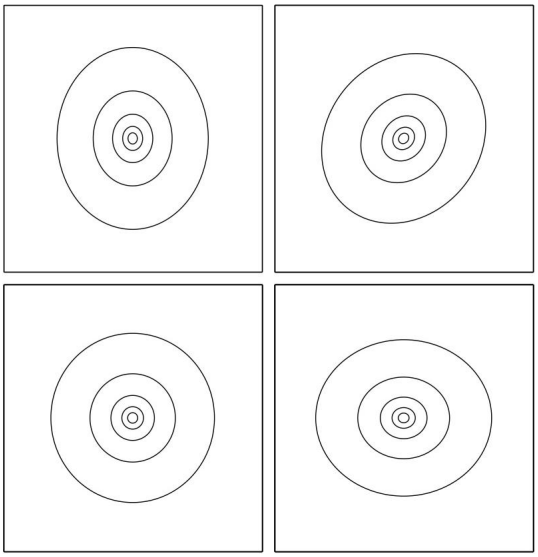

(a) PIEMD in 20×20 kpc box.

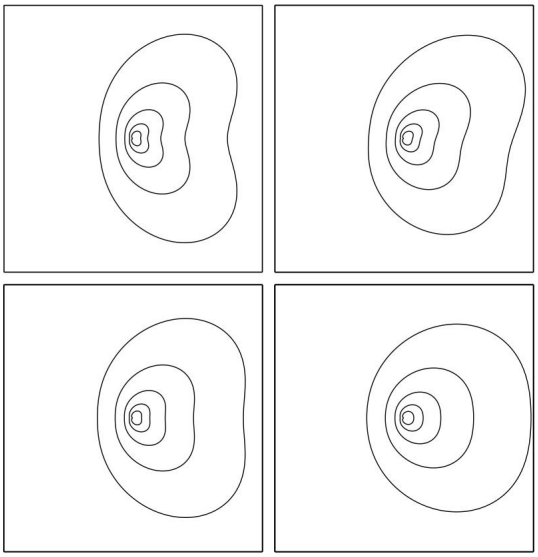

(b) PISP with large skew to the right.

Figure 7: This is the same as Figure 6, but now a much bigger skew, $s = 0.5$, is taken. This induces apparent ellipticities that are not present in the unskewed lenses. For this reason, large skews should be avoided for PISPs.

the same point when they share the same parameters, excluding skew. This is convenient since the output of Lenstool can then be used as the true peak.

I tested the PISP to ensure that it does not incorrectly predict skew, when none is present, using the *Example with Images* simulation, available with Lenstool, with a prior of $s \in [0.3, -0.3]$. This recovers a best fit of $s = -0.0008^{+0.02}_{-0.02}$. For comparison, when modelling the galaxies in Abell 3827 skews were found to be as large as $O(0.1)$.

I also tested the PISP on simulations of lenses with non-zero skews. Choosing one member from each multiply-lensed image family in the *Example with Images*, I projected the light back through a PISP, with a skew of $s = 0.2$ and a skew angle of $\phi_s = 1.6$, with all other parameters the same as the default simulation. This determined the source positions. By projecting the light back through the lens, I generated a mock data set of multiply lensed images. Running Lenstool on this mock data recovered $s = 0.2^{+0.001}_{-0.001}$ and $\phi_s = 1.6^{+0.04}_{-0.05}$.

Finally I performed a test on a mock cluster lens, based on the cluster Abell 3827. Choosing one of the quadruply lensed background galaxy images, I repeated the procedure outlined above, projecting the light backwards and then forwards through the cluster lens. The cluster was given the same parameters as the fiducial model for Abell 3827, discussed later in this thesis, with the exception of the skew parameters. In this simulation the galaxies N2-N4 were set to have no skew, with $s = 0$. Galaxy N1 was taken to be skewed, with $s = 0.25$ and $\phi_s = 1.6$. I then ran Lenstool with the same free parameters used to model Abell 3827 (see Section 6 for more details).The resulting posterior is shown in Figure 8. The peak of the posterior is a fairly accurate estimator for the true skew, however the error bars remain large. The numerical results are summarised in Table 1.

All tests were done using Lenstool runmode 3 to fully explore the posterior. Going forward I will use the peak of the posterior to estimate the true skew, and not the best fit value, as in this simulation the best fit value was incorrect by $\sim 180°$. The fact that the best fit values and posterior peak do not coincide, is not fully unexpected, as although we have flat priors on each of our parameters, these are not necessarily the parameters of physical relevance (e.g. we place a flat prior on the velocity dispersion, σ_0, and not σ_0^2 which is proportional to the mass of the cluster).

Table 1: Summary of the results of the simulation. For each galaxy the input skew and skew angle are given by, s_{true} and $\phi_{s_{true}}$, respectively, whilst the posterior peak is given by $\hat{s}$ and $\hat{\phi}_s$.

Galaxy	s_{true}	$\phi_{s_{true}}$	$\hat{s}$	$\hat{\phi}_s$
N1	0.25	1.60	$0.24^{+0.04}_{-0.31}$	$1.6^{0.92}_{-0.99}$
N2	0.0	NA	$0.01^{+0.14}_{-0.13}$	$2.5^{+0.37}_{-1.5}$
N3	0.0	NA	$0.07^{+0.10}_{-0.15}$	$2.3^{+0.5}_{-1.56}$
N4	0.0	NA	$0.11^{+0.11}_{-0.16}$	$1.4^{1.04}_{-0.88}$

3.6 A Note on Parameter Space Exploration and Priors

Any skew can be expressed as a vector, in a two dimensional skew parameter space, determined by the direction and magnitude of the skew. When introducing skewed distributions into Lenstool one faces a choice: to express this vector in polar or Cartesian

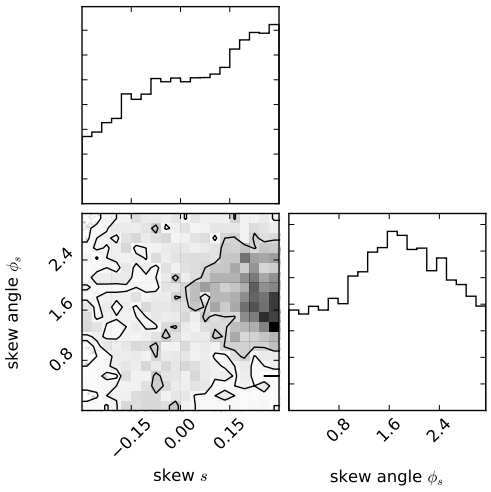

(a) Galaxy N1

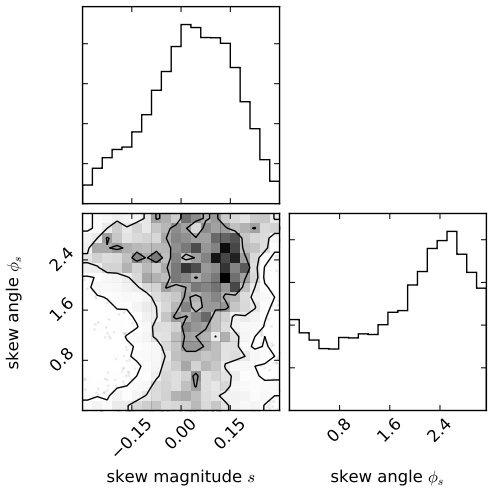

(c) Galaxy N2

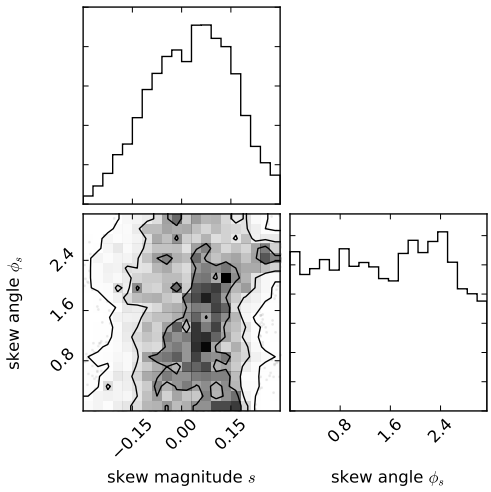

(e) Galaxy N3

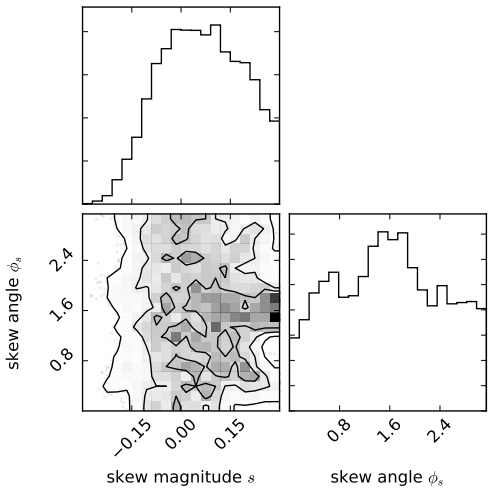

(g) Galaxy N4

Figure 8: The posterior of the skew and skew angle of four central elliptical galaxies in a simulated galaxy cluster lens, recovered from 10,000 points. Lines indicate the 1σ, 2σ and 3σ confidence levels. With the exception of the skew parameters, the true parameters are the same as the fiducial model discussed later. The true skew values are $s = 0.25$ and $\phi_s = 1.6$ for galaxy N1, and $s = 0$ for galaxies N1-N3. The peak of the posterior recovers the true parameters accurately, but with large uncertainty.

coordinates. I chose the former. This is because the MCMC can then explore a circularly symmetric region which will not bias the skew direction. If I had instead chosen to express the skew in Cartesian coordinates, the MCMC chain would explore a square region favouring skew vectors that point towards the corner of the priors.

My choice does not come without problems. What we are actually trying to compute is the posterior of the skew in the direction of the stellar to dark matter offset. I now outline the procedure for converting the posterior of the skew and skew angle, as computed by Lenstool, to the posterior of the skew in the direction of the offset.

I convert all skew vectors from polar space, defined by their skew and skew angle, into Cartesian space, defined in x and y, where I take the best fit offset direction as the x-axis, and the direction orthogonal to this as the y-axis. The maps between these two spaces are not area preserving, and since we are concerned with the probability density we must weight all points by the magnitude of the skew, $|s|$, to account for the Jacobian.

There is a further complication in transforming the posterior between these two spaces. This is because when I run Lenstool, I specify a flat prior on both the skew and skew angle. This is not the same as specifying a flat prior on the x-direction skew. This can be seen in Figure 9a-9b. In the former figure I have drawn 10,000 points uniformly from the priors set in Lenstool, for skews $s \in [-0.3, 0.3]$. In Figure 9b I have converted this prior into Cartesian space taking into account the Jacobian. As can be seen this prior is not flat in the x-direction because we are preferentially choosing points near $x = 0$ where the circle, giving the prior boundary in parameter space, is thickest. This biases the posterior away from large skews in the x-direction.

What we really want is a flat prior on the x-direction skew. This can be done by taking the posterior of the x-direction skew, computed by Lenstool, and multiplying it by the inverse of the prior shown in Figure 9b to find the likelihood. Taking this likelihood as the posterior for x-direction skew is equivalent to giving the skews in the x-direction a flat prior. In particular we note that weighting all points by:

$$\frac{1}{\sqrt{0.3^2 - x^2}} \tag{49}$$

to account for the thickness of the circle is equivalent to multiplying by the inverse of the prior. This can be seen in Figure 9c where I have performed this weighting to the prior shown in Figure 9b, to recover a flat prior for the projected skew in the x-direction.

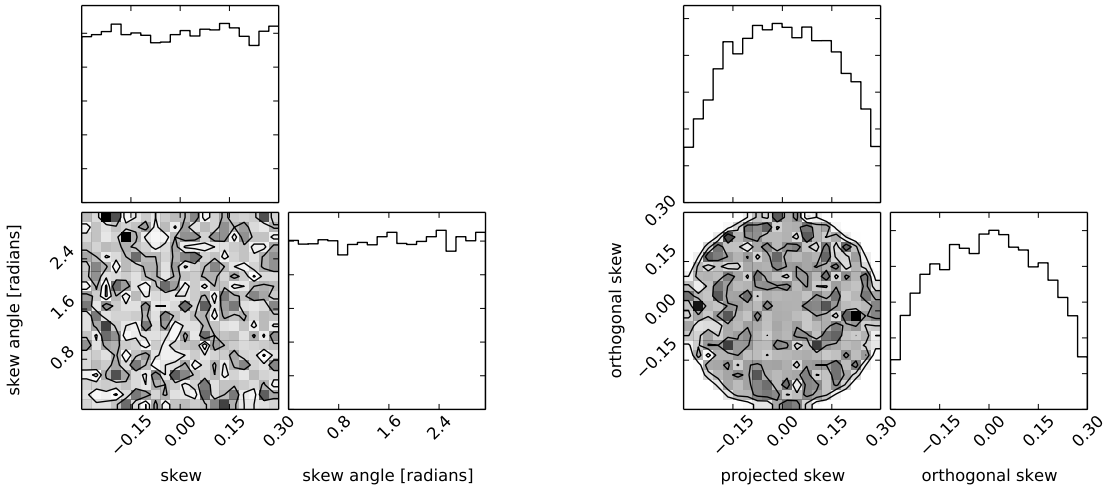

(a) (b)

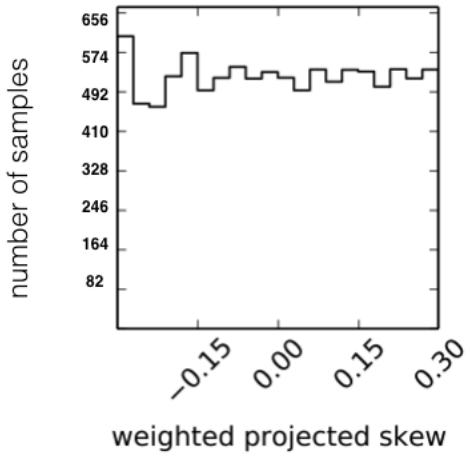

(c)

Figure 9: In (a), 10,000 points drawn randomly from the prior set in Lenstool which is a flat prior on the skew and skew angle. In (b), data points are from the same sample as shown in (a), but now projected into Cartesian space. The Jacobian has been accounted for when transforming between these two spaces. In (c), I marginalise over the orthogonal skew, and weight the points according to equation 49. This recovers a flat prior for the projected skew.

4 Abell 3827 Existing Modelling and New Data

In this section mass models using the new skewed lenses are developed. Existing data and mass modelling of the cluster Abell 3827 are discussed first, before moving on to discuss the new MUSE data and its inclusion into the lens modelling. This is followed by a discussion of other improvements that can be made to the lens model presented in [34]. Finally the cluster is modelled with skewed lenses, and possible physical interpretations are discussed. A cosmology of $\Omega_M = 0.3$, $\Omega_\Lambda = 0.7$ and $H_0 = 70$ km s^{-1} Mpc^{-1} is assumed throughout, so that $1''$ corresponds to 1.828 kpc at the redshift of the cluster.

Models are compared by three objective measures. These are image plane r.m.s defined as:

$$\langle r.m.s \rangle = \sqrt{\frac{1}{N}\sum_i \left[x^i_{observed} - x^i_{predicted}\right]^2}, \tag{50}$$

where i is the ith multiple image and N gives the total number of multiple images. The χ^2 is given by:

$$\chi^2 = \sum_i \frac{\left[x^i_{observed} - x^i_{predicted}\right]^2}{\sigma_i^2}, \tag{51}$$

where σ_i is the error on each image position. Finally, we can define:

$$\chi^2/\mathrm{dof} = \frac{\chi^2}{N-n} \tag{52}$$

where n is the number of independent optimised parameters.

It is important to note that in some of the models the r.m.s and χ^2 will not go up in lockstep as is usually expected. This is because the constraints from *Hubble* and VLT/MUSE are assigned different errors σ_i, due to *Hubble's* superior angular resolution.

4.1 The Cluster Abell 3827 and Existing Work

Abell 3827 is a perfect laboratory to study DM self-interaction. A HST image of the centre of Abell 3827 is shown in Figure 10 where one can see four bright ellipticals within the central 20 kpc. Such mass corrugation is unrivalled [34]. Additionally, the core is ideally placed in front of a multiply lensed background source, allowing the cluster's mass distribution to be reconstructed.

The first mass reconstruction of this system was performed in [44], using ground based imaging. An offset of $\sim 3''$, or ~ 6 kpc, was found between the local mass peak and luminosity peak in galaxy N1. Using HST data this model has been refined in [34]. Multiple knots of star formation were identified and are shown in Figure 11.

Using these constraints, the mass was modelled using the parametric lensing software, Lenstool, and a non-parametric package Grale. Both found an offset of $\sim 1.5''$, or ~ 3 kpc, in galaxy N1 in the southeasterly direction.

The model constructed with Lenstool serves as a starting point for the mass models constructed in this thesis. The assumptions and modelling procedure used in the Lenstool mass reconstruction are now outlined.

In this model the error on the positions was assumed to be $0.2''$, bounded by the finite angular resolution of HST. The parameter BayesRate, which sets the convergence time of the MCMC was set at 0.1. For more information about the BayesRate parameter see [20]. Galaxies N1-N4 and N6 were all modelled with PIEMDs. The position,

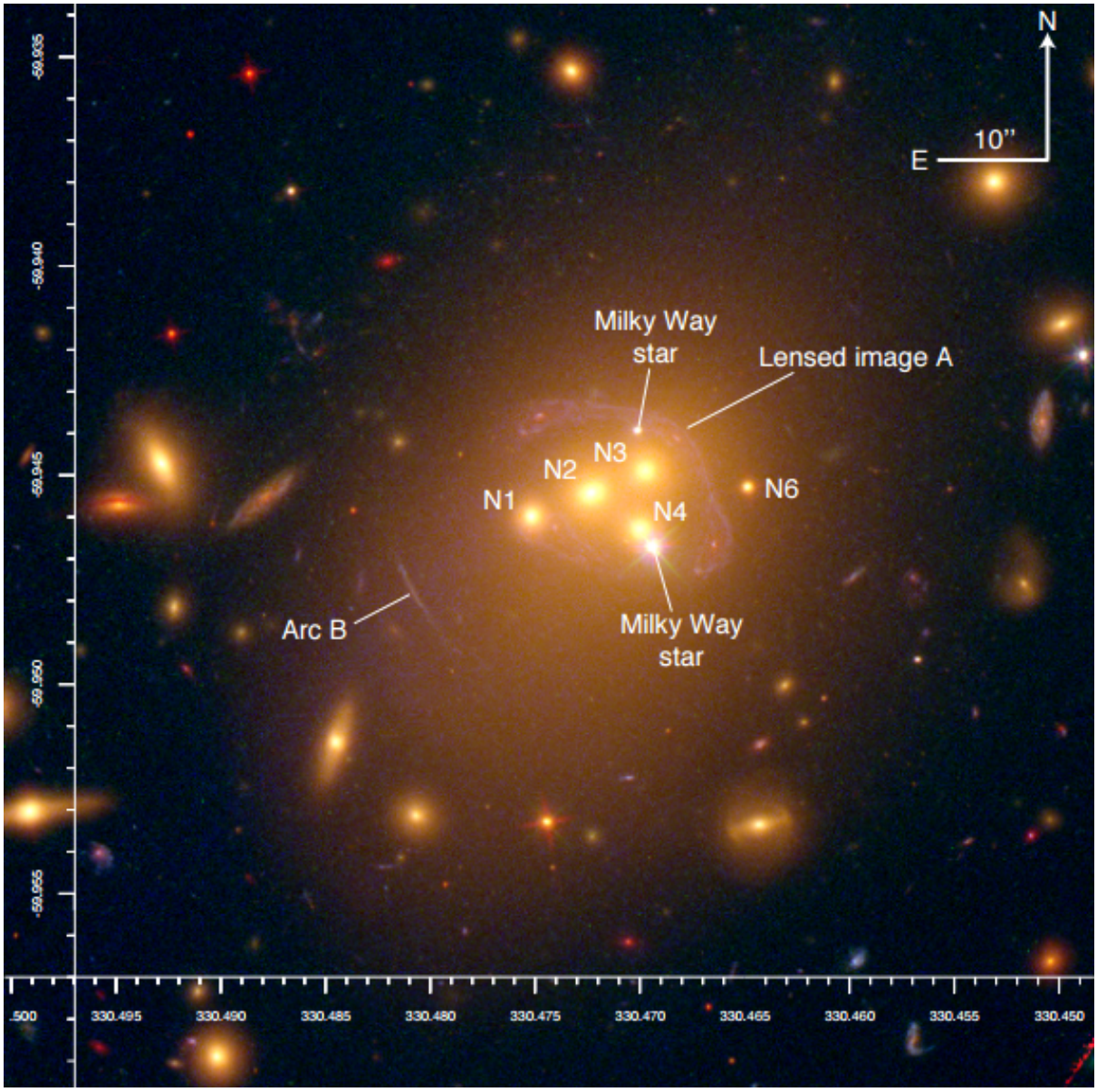

Figure 10: *Hubble Space Telescope* image of Abell 3827. This is a stacked image showing the F160W, F606 and F336 colour bands. The colour scale is logarithmic. N1-N4 label the four central bright elliptical galaxies. This figure is adapted from [34].

ellipticity, orientation and velocity dispersion were left free in galaxies N1-N4. Only the velocity dispersion was optimised in galaxy N6, since it is much less massive than the others. Finally the position, ellipticity, orientation, core radius and velocity dispersion were optimised in the cluster scale halo.

As the position of N1 was expected to be well constrained, as it is surrounded by many lensed knots of star formation, flat priors were set within $-5'' < x < 3''$ and $-3'' < y < 3''$, where the position of the luminosity peak is $(x, y) = (-0.06, 0.04)$. The position of galaxies N2-N4 were expected to be less well constrained, so these were given Gaussian priors with $\sigma = 0.5''$. The position of the cluster scale halo was given a Gaussian prior with $\sigma = 2''$, or 3.66 kpc, centred near the position of galaxy N2. The ellipticity

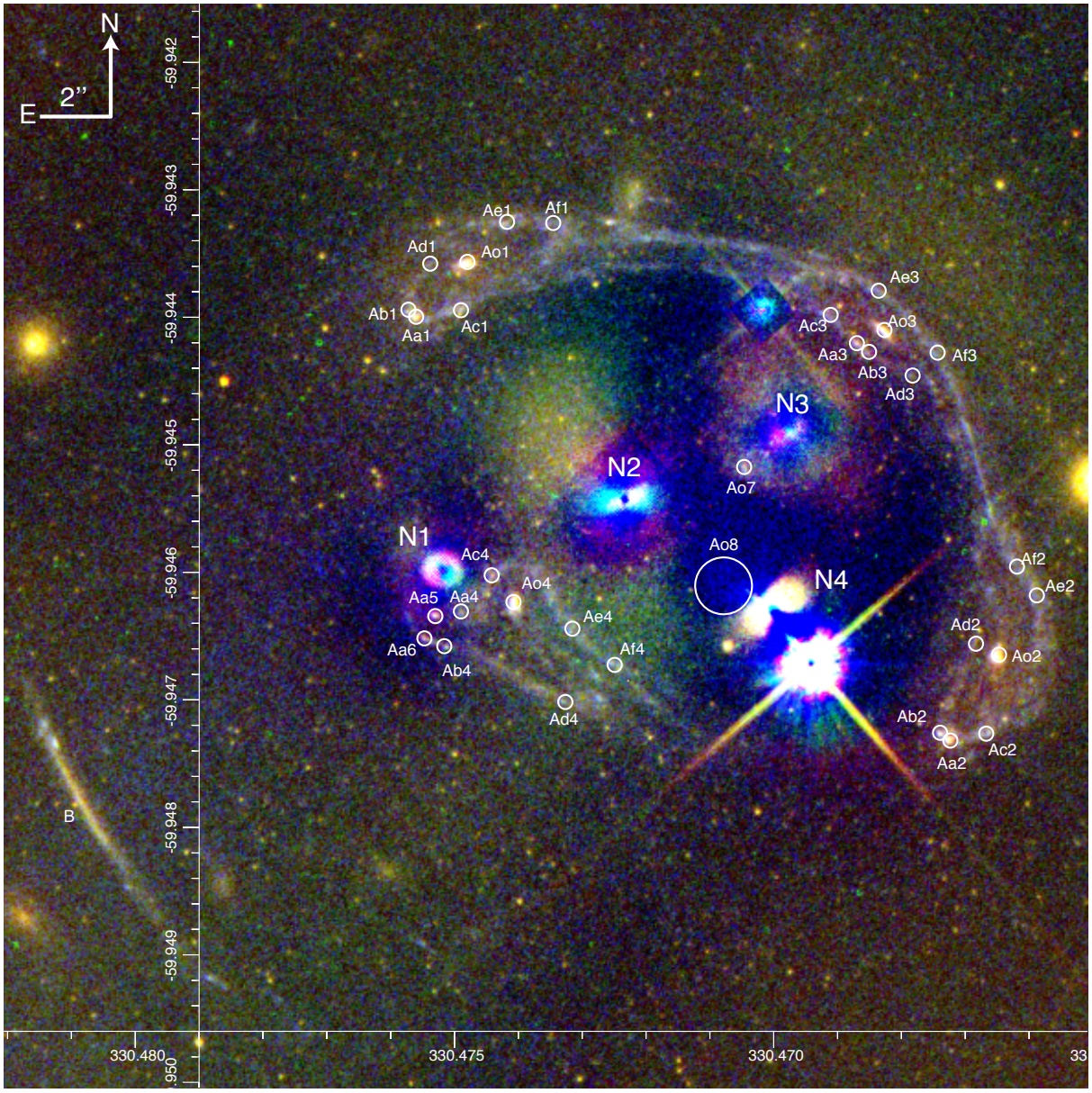

Figure 11: Foreground subtracted HST image showing the final multiple image identifications. The radius of the circles gives the uncertainty of the image position used in Lenstool. All multiple images were previously identified in [34], except images Aa8 and Aa7, which were identified in this work. This figure is adapted from [34].

defined as:

$$e = \frac{a^2 - b^2}{a^2 + b^2} \tag{53}$$

is given a flat prior with $e < 0.45$ for galaxies N1-N4. The ellipticity of the cluster scale halo is given a flat prior with $e < 0.75$. The velocity dispersion for galaxies N1-N4 and the cluster scale halo are all given flat priors. Additionally the cut radii are fixed for the galaxy scale halos to be $100''$, or 182.8 kpc, well outside the strong lensing region. Finally the cut radius of the cluster scale halo is taken to be $1000''$. The core radius of galaxies N1-N4 is taken to be $0.1''$, and the core radius of the cluster scale halo is given a flat prior, $r_{core} < 40''$. The recovered best fit parameters are shown in Figure 13. This model achieves an image plane $\langle r.m.s \rangle = 0.26''$, $\chi^2 = 49.3$ and $\chi^2/\text{dof} = 2.14$.

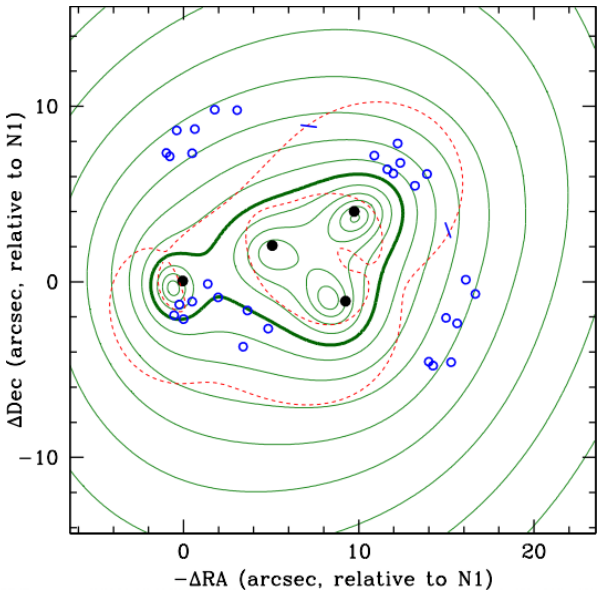

Figure 12: The best fit mass map of Abell 3827 given in [34]. Green contours show the density and are logarithmically spaced by a factor of 1.5. The blue circles show the position of the multiply-lensed images and the black dots show the location of the luminosity peak. The offset in galaxy N1 is clearly present. There are also visible offsets in the other galaxies but these are poorly constrained in this model. Figure is taken from [34]

	σ_v [km/s]	x [″]	y [″]	e	θ [°]	r_{core} [″]	$\langle rms_i \rangle$ [″]	χ^2/dof	$\log_{10}(E)$
Fiducial model:							0.26	49.3/23	−26.4
N.1	190^{+8}_{-12}	$-0.61^{+0.14}_{-0.12}$	$-0.46^{+0.20}_{-0.14}$	$0.25^{+0.15}_{-0.04}$	101^{+22}_{-22}	[→0]			
N.2	219^{+18}_{-38}	$-0.13^{+0.28}_{-0.46}$	$-0.48^{+0.30}_{-0.30}$	$0.09^{+0.12}_{-0.09}$	174^{+22}_{-37}	[→0]			
N.3	254^{+17}_{-14}	$0.09^{+0.25}_{-0.25}$	$-0.36^{+0.18}_{-0.29}$	$0.25^{+0.04}_{-0.10}$	30^{+11}_{-13}	[→0]			
N.4	235^{+20}_{-34}	$-0.99^{+0.39}_{-0.34}$	$-0.01^{+0.35}_{-0.27}$	$0.19^{+0.12}_{-0.09}$	121^{+22}_{-54}	[→0]			
N.6	18^{+44}_{-1}	[0]	[0]	[0]	[0]	[→0]			
Cluster	620^{+101}_{-58}	$6.18^{+1.33}_{-1.04}$	$2.30^{+1.86}_{-1.51}$	$0.70^{+0.01}_{-0.24}$	61^{+3}_{-4}	$30.12^{+9.23}_{-6.43}$			

Figure 13: The best fit model parameters found in [34]. Positions are relative to the luminosity peaks of the nearest galaxy, except the cluster-scale-halo, which is relative to the luminosity peak of N1. This figure is taken from [34].

4.2 New Data and MUSE Data Reduction

New VLT/Muse observations of Abell 3827 were taken on the 25 and 26 of June 2015. The data were reduced by Mark Swinbank using v1.2.1 of the ESOREX pipeline to form a data cube. To subtract the light from the foreground galaxies, a polynomial was fitted to the spectrum within 200 Å ignoring a 15 Å region either side of the emission line. The fitted spectrum was then subtracted from the entire data cube, revealing the background galaxies in a 15 Å region about the OII line, and in particular, the previously unseen demagnified images can be identified, as shown in Figure 14.

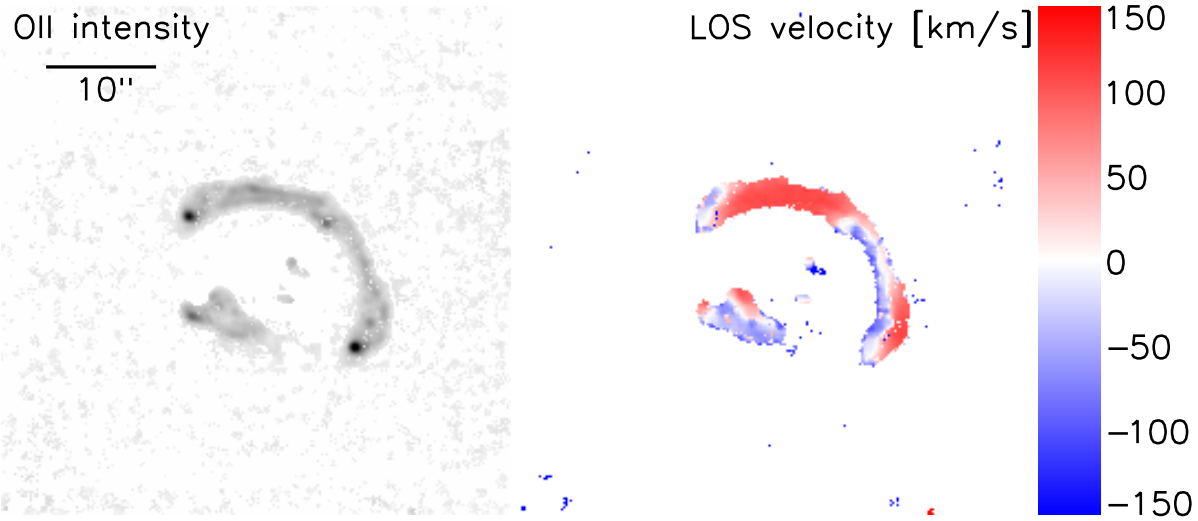

Figure 14: Muse image after foreground subtraction. The left panel shows the OII emission line intensity, and the right panel shows the line of sight velocity, which can be used to match up different parts of the image. Two previously unseen demagnified images can be seen near the centre right of the ring. This is particularly clear in the OII intensity map. Image credit: Mark Swinbank.

5 Lens Modelling

5.1 Flat Priors on the Position

The model in [34], discussed earlier, takes the position of galaxy N1 to have a flat prior and the position of all the other galaxies to have Gaussian priors. The reasoning is that this fixes the position of the other galaxies more tightly, so that the position of N1, which is assumed to be most well constrained, due to its angular proximity to a large number of constraints, can be explored more accurately. The problem with this line of reasoning is twofold. Firstly, the position of the source should not influence our choice of prior. If we are looking for evidence of SIDM, and say that we are uncertain about the position of one galaxy giving it a flat prior, then *all* galaxy positions are uncertain and should be given flat priors. Secondly, giving only galaxy N1 a flat prior could transfer the freedom in the model from potential offsets in other galaxies to the position of N1, causing us to overestimate the true offset in galaxy N1 and miss potential offsets in the other galaxies. For this reason I give galaxies N1-N4 flat priors in a $4'' \times 4''$ boxes centred on the respective luminosity peaks of each galaxy.

I decrease the cut radii of galaxies N1-N4 to $40''$ (73.1 kpc), since the cut radii given in [34] are aphysically large as the total mass of the halo is proportional to the cut radius. For a more complete discussion on typical galactic cut radii in clusters see [31].

Finally the prior on the ellipticity is widened to $e < 0.5$ and the MCMC convergence rate is set to bayesRate = 0.02. This is done preemptively to keep the bayesRate consistent across models, since when skew is considered, the MCMC burn-in phase may need to be longer to explore a larger parameter space.

Giving all the galaxies flat priors leads to a greater than 3σ detection of an offset in galaxy N4, while the offset in galaxy N1 remains effectively unchanged. The best fit offset measured in galaxy N4 is $\sim 2.9 \pm 0.6$ kpc.

This model achieves an image plane $\langle r.m.s \rangle = 0.25$, a $\chi^2 = 48.75$ and a reduced $\chi^2/\text{dof} = 2.12$. This is an extremely modest and non statistically significant improvement to the original model. However, this model does predict that there should be two demagnified images of the entire background galaxy where the MUSE detections are observed. In contrast, the model presented in [34] only predicts one extended demagnified image lying approximately 3.5 kpc to the East of where the MUSE detections are actually observed.

5.2 Adding the Stellar Mass

I model the stellar mass of the four central bright galaxies separately from the DM component for two reasons. Firstly, it was found in [14] that modelling this separately can improve the r.m.s of mass models in galaxy clusters. Secondly, this limits the possibility that unaccounted for stellar mass is responsible for any detected skew.

As in [13], the stellar halos are modelled with Hernquist profiles where:

$$\rho_{\text{star}}(r) = \frac{\rho_s}{(r/r_s)\,(1 + r/r_s)^3}. \tag{54}$$

The scale radius is related to the half mass radius R_e as $r_s = 0.551\ R_e$. The scale density ρ_s is given by

$$\rho_s = \frac{M_{\text{star}}}{2\pi r_g^3}. \tag{55}$$

For galaxies N1-N4, I take the stellar mass component estimated in [34], and take the half mass radius to be the effective radius found in Galfit [36]. These parameters are given in Table 2.

Table 2: The stellar mass parameters given from left to right are: galaxy ID, mass, scale radius, ellipticity and orientation. Masses are computed from the F606W band magnitudes. See [34] for more details. The ellipticity, scale radius and orientation are computed using Galfit. The stellar component of galaxy N4 has significantly different parameter values from the others, suggesting stellar light contamination from the nearby Milky Way star.

Galaxy	Mass[$M_\odot$]	$r_{cut}['']$	e	$\theta[^\circ]$
N1	1.00×10^{11}	.529	.12	61
N2	2.46×10^{11}	.789	.17	39
N3	2.77×10^{11}	.332	.05	31
N4	2.08×10^{11}	1.37	.39	127

This model achieves an image plane $\langle r.m.s \rangle = 0.24$, a $\chi^2 = 45.07$ and $\chi^2/\text{dof} = 1.96$ This is again a modest improvement, but the main purpose of including the stellar mass is to ensure that any detection of skew is not caused by stellar mass that is not accounted for separately.

5.3 Adding the Northern MUSE Source

Using the methods presented in [19], a new foreground subtracted image has been produced by Rémy Joseph. This reveals an additional counter-image between galaxies N3 and N4. Although first unambiguously revealed by the MUSE data, in hindsight, it is also faintly visible in the HST foreground subtracted image shown in Figure 11. The superior angular resolution of HST means an image position error of 0.2 can be used, helping to more tightly constrain the position of the nearby galaxies N3 and N4, than would be possible with the MUSE data alone.

The brightest knots of star formation are the Aa, Ao and Ab families, as shown in Figure 11. The newly identified demagnified image is likely one of these. I have modelled all three possibilities separately in Lenstool and the results are summarised in Table 3. Although the Ao model gives the lowest χ^2, it is essentially indistinguishable from the Aa model. In all three cases the entire background galaxy is expected to be lensed onto both the upper and lower MUSE images. However, as the number of times an image is lensed must be odd a third image is expected. In the Aa model this third image is expected to lie directly behind galaxy N3. As the foreground subtraction is imperfect in such a high flux area of the image, this would explain why no third demagnified image is seen in the MUSE data. For this reason I choose to identify this image with the family Aa.

5.4 Adding the Southern MUSE

Finally I add the lower VLT/MUSE source to the model. The previous model predicts that another image of the Aa family source should lie near the centre of the MUSE image, so I identify this with the lower image. As MUSE's angular resolution is worse than HST's, I give this source an error of $\sigma = 0.8''$ as opposed to $\sigma = 0.2''$ like the others. From equation 51, this acts to down-weight the contribution to the χ^2 by a factor of 16.

Table 3: Comparison of different Lenstool models where different image families are chosen to correspond to the upper source in the MUSE image

Image Family	χ^2	$\langle r.m.s \rangle$ [$''$]	χ^2/dof
Aa	$44.99^{+6.7}_{-6.5}$	.24	1.80
Ab	$49.40^{+7.5}_{-4.7}$	.25	1.98
Ao	$44.00\ ^{+7.2}_{-5.8}$	.24	1.76

This model achieves $\chi^2 = 51.11$, $\langle r.m.s \rangle = 0.25$ and $\chi^2/\text{dof} = 1.89$.. The main improvement compared to the previous model comes from further constraining the position of galaxy N4 which initially had error of $\sim 0.25''$ and $\sim 0.35''$ in the x and y directions respectively, but these errors are reduced to $\sim 0.1''$ and $\sim 0.15''$ with the addition of the southern MUSE source.

5.5 Modelling Galaxies N1-N4 with the PISP

Finally, I construct a model where each of the four central galaxies are taken to be PISPs. The skew and skew angle are given flat priors with $s \in [-0.3, 0.3]$, ensuring that the skew does not overwhelm the inherent ellipticity, as discussed in Section 3.5. This model is taken as the fiducial model in this thesis. The final multiple image identifications are shown in Figure 11. The cumulative density map is shown in Figure 15 and the density contours for each galaxy separately, are show in Figure 16. Finally, the posterior for galaxies N1-N4 can be seen in Figures 17-20, which are produced using the Python module Corner [12].

This model achieves $\chi^2 = 51.24$, $\langle r.m.s \rangle = 0.26$ and $\chi^2/\text{dof} = 2.70$. Introducing skew makes no difference to the r.m.s, and actually makes the reduced χ^2 worse, as so many new parameters have been introduced.

5.6 Summary of Mass Models

A comparison between the different lens models presented here are given in Table 4. Details of further models, and robustness checks can be found in the appendix.

Table 4: A summary of all the models presented in this section. The name of the model describes what has been added in comparison to the previous model in the list.

Model	χ^2	$\chi^2/d.o.f$	r.m.s [$''$]
Model presented in [34]	49.3	2.14	0.26
Flat Priors on Position	48.75	2.12	0.25
Stellar Mass	45.07	1.96	0.24
Northern MUSE Source	44.99	1.80	0.24
Southern MUSE Source	51.11	1.89	0.25
Fiducial Model	51.24	2.70	0.26

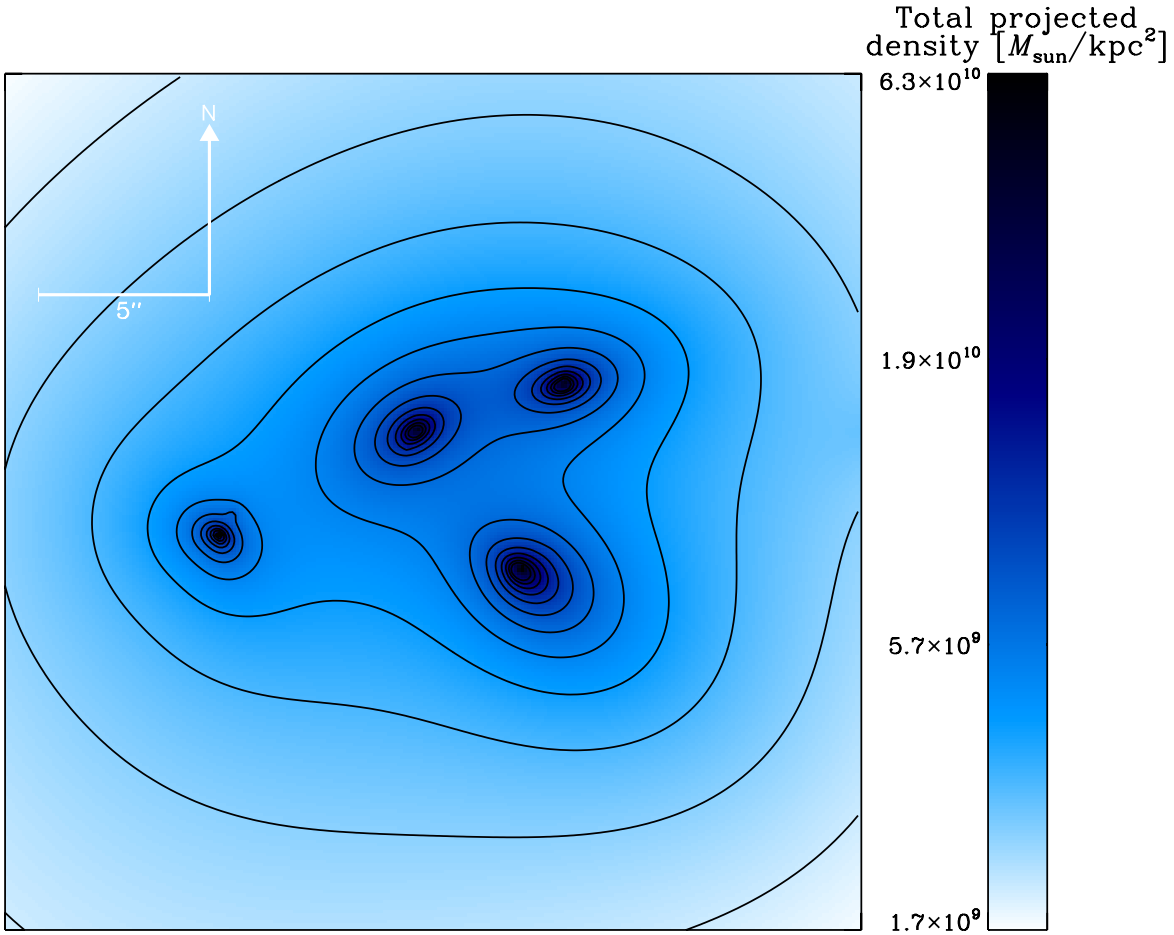

Figure 15: Isodensity contours for fiducial mass model including skew. The outermost contour corresponds to a projected density of 2×10^9 $M_\odot$/kpc^2, and values logarithmically increase by a factor of 0.1 towards the centre. Image credit: Richard Massey.

6 Discussion and Physical Interpretation

6.1 General Findings

A 3σ detection of an offset in galaxies N1 and N4 persists in the fiducial model, consistent with the models without skew. Importantly the offset measurements with and without skew are similar, suggesting that the measured position of the density peak is insensitive to the exact shape of the DM halo. This can be seen in Figures 21-22. However, the uncertainty in the position of the peak does become larger when we account for the possibility of a skewed DM halo with the PISP.

There is also tentative evidence of a skew in galaxy N1, in a direction that is consistent with the SIDM interpretation. However, there is no evidence of a similiar skew in the other offset galaxy, N4, as although skew is present in the best fit model, there is no evidence for skew in the shape of the posterior. This can be seen in Figure 20. As expected, there is little sign of a skew in the galaxies N2 and N3, where no offset is present.

I now present the results in slightly more detail and provide an interpretation for the recovered offsets and skew parameters, before estimating the cross-section of DM, from the offset measurements in galaxies N1 and N4.

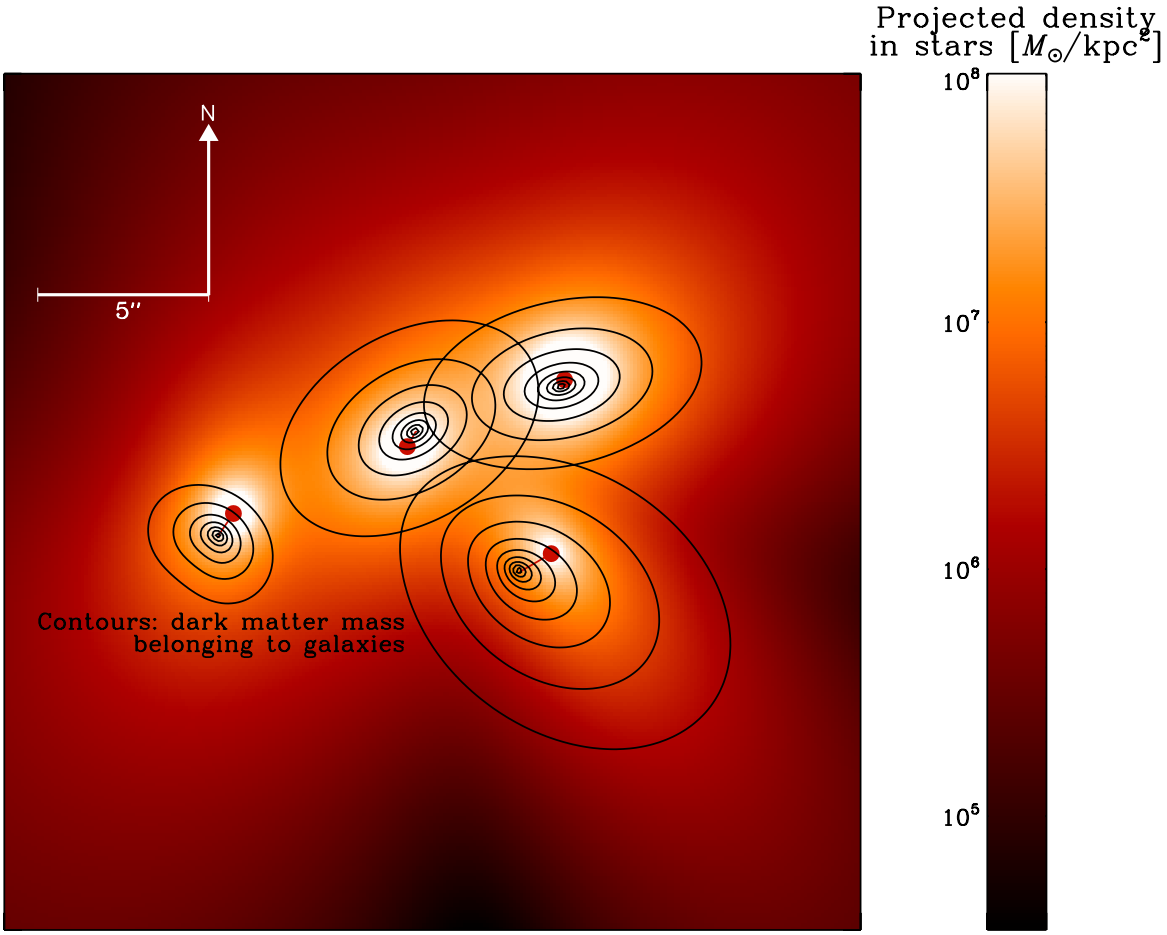

Figure 16: Isodensity contours for each individual galaxy in the fiducial mass model. A skew is notable in galaxy N1 and is consistent with the SIDM interpretation. Skews in the other galaxies are not favoured by the posterior and are not statistically significant. Red dots indicate the centre of the luminosity peak. Offsets are clearly visible in galaxies N1 and N4, while the offset in galaxy N2 is not statistically significant. The outermost contour corresponds to a projected density of $1\times10^{9.1}$ $M_\odot$/kpc^2 and values logarithmically increase towards the centre by a factor of 0.2. Image credit: Richard Massey.

6.2 Galaxy N1

There is tentative evidence that the DM halo of galaxy N1 is skewed in a direction that is consistent with the SIDM interpretation for the offsets. This can be seen in Figures 23-24. On the left hand side of Figures 23, I project the skew vector, defined by the skew and skew angle, onto the vector pointing from the DM peak to the stellar luminosity in the fiducial model, so that a positive skew corresponds to the direction predicted by SIDM. On the right hand side of this figure I project the skew vector onto the offset vector between dark and luminous matter for each step in the MCMC. As can be seen, there is little difference between these two projections, and in both cases $\sim 75\%$ of the posterior lies to the right of 0. In Figure 24a, I weight the points in Figure 23a, to account for the fact that the prior biases the posterior away from large skews, as discussed in Section 3.6. This weighting has little effect on the resulting posterior. Most of the skew is in the direction of the offset. This can be seen in Figure 24b where I have projected the skew vector onto a vector orthogonal to the offset direction, and reweighed the points to

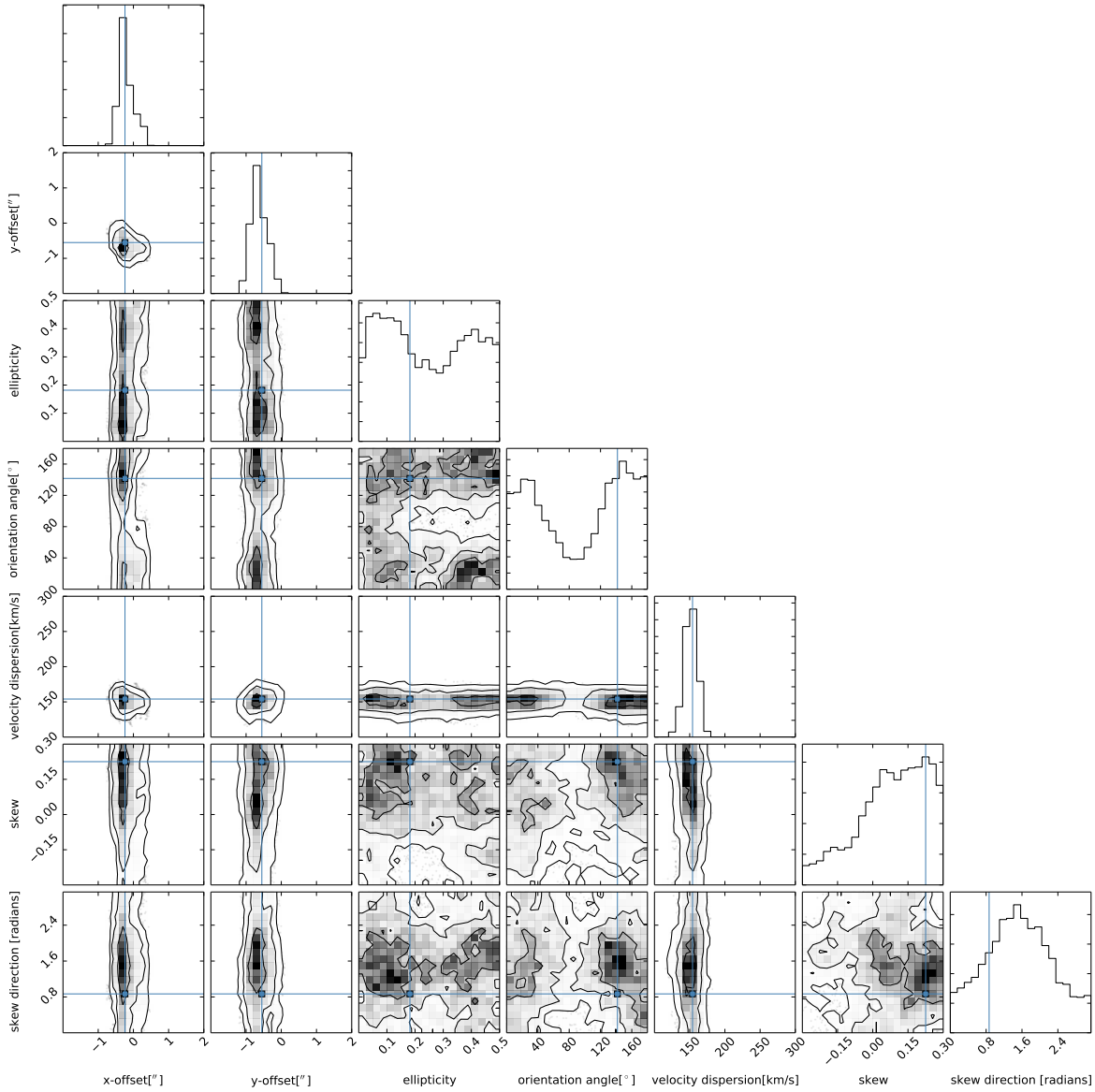

Figure 17: Posterior probability, from 10,000 samples, for parameters of galaxy N1, with contours showing the 1σ, 2σ and 3σ contour levels. The best fit model parameters are indicated in blue. The position has been rescaled so that $(x, y) = (0, 0)$ corresponds to the luminosity peak in galaxy N1. An offset is measured at the 3σ level. Intriguingly the skew angle is consistent with the SIDM interpretation. Large skews are also favoured, but the results are still statistically consistent with $s = 0$. The skew angle is defined anticlockwise from West.

take account of the small skew bias. The resulting posterior is centred about 0, and on comparing Figures 24a and 24b it can be seen that most of the devition from zero skew in the posterior, is in the direction parallel to the offset, just as would be expected from the SIDM interpretation.

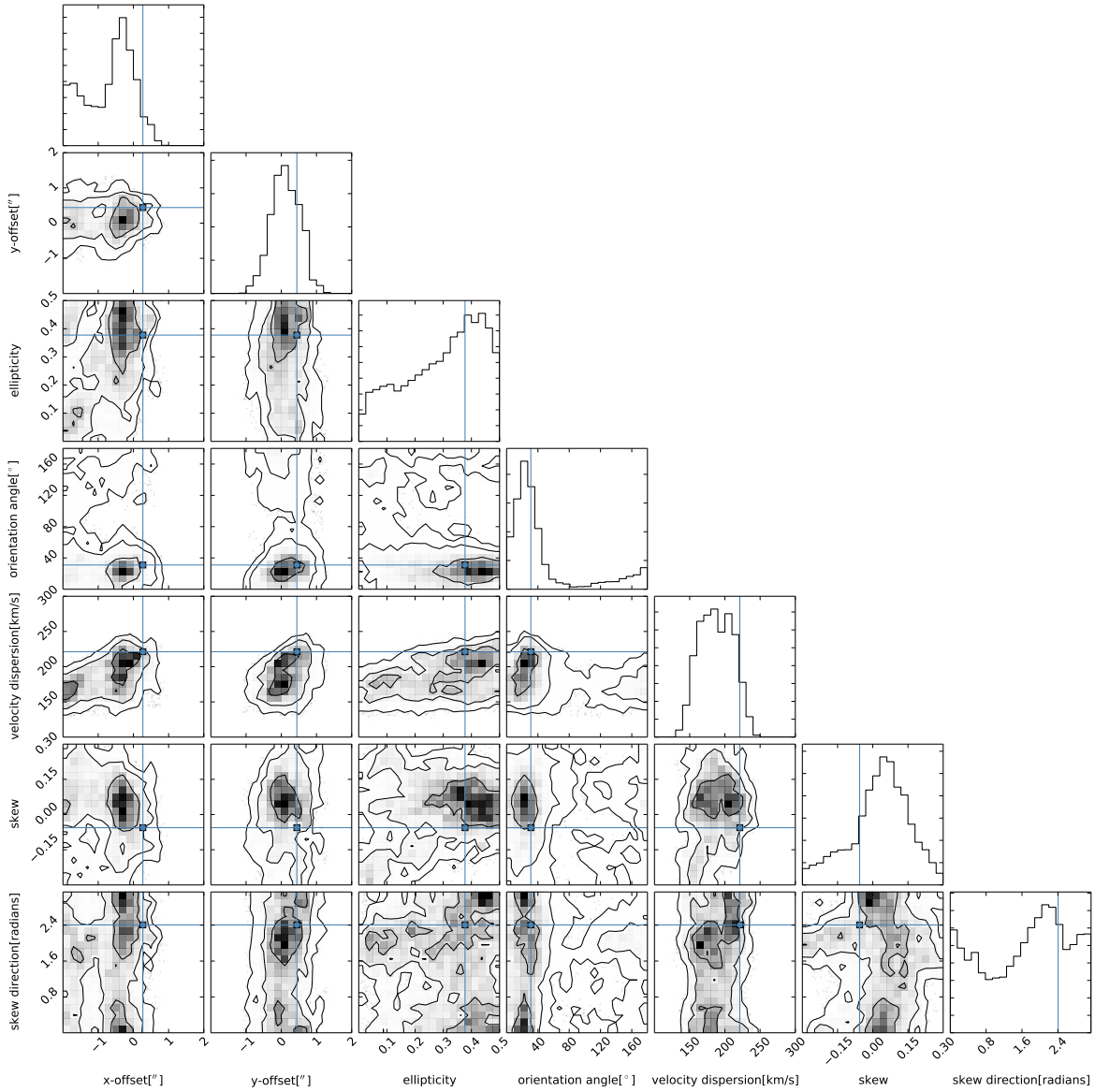

Figure 18: Posterior probability, from 10,000 samples, for parameters of galaxy N2, with contours showing the 1σ, 2σ and 3σ contour levels. The best fit model parameters are indicated in blue. The position has been rescaled so that $(x, y) = (0, 0)$ corresponds to the luminosity peak in galaxy N2. Of the four central galaxies, the position of N2 is the least well constrained. Small skews consistent with elliptical symmetry are preferred as expected since there is no evidence for an offset in galaxy N2. The skew angle is defined anticlockwise from West.

6.3 Galaxies N2 and N3

There are no indications of offsets or skews in galaxies N2 and N3. This can be seen in Figures 18 and 19. If DM self-interactions are responsible for the offsets in the other galaxies, there are two possibilities for why they are not observed in galaxy N2 and N3. The first, is that these galaxies have smaller velocities orthogonal to the line-of-sight. This possibility does not preclude offsets from existing along the line-of-sight, which would not be detected, as we can only probe the projected mass. The other option, is that galaxies

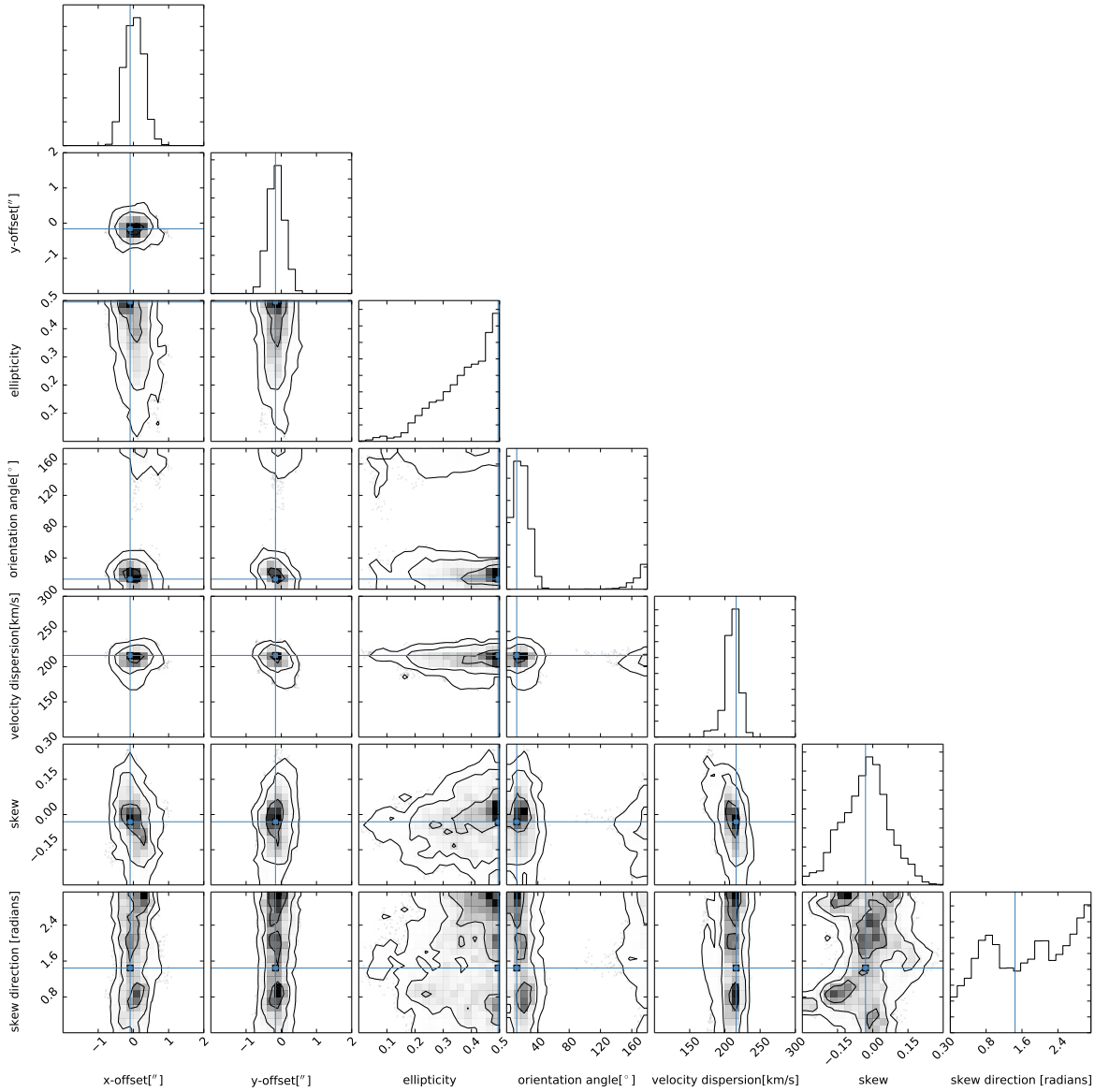

Figure 19: Posterior probability, from 10,000 samples, for parameters of galaxy N3, with contours showing the 1σ, 2σ and 3σ contour levels. The best fit model parameters are indicated in blue. The position has been rescaled so that $(x, y) = (0, 0)$ corresponds to the luminosity peak in galaxy N3. Small skews consistent with elliptical symmetry are preferred. This is expected as there is no discernible offset in galaxy N3. The skew angle is defined anticlockwise from West.

N2 and N3 are spatially separated, along the line-of-sight, from the high density regions at the cluster core. This would also explain the lack of offsets, as DM particles in halos travelling through lower density environments are less likely to be scattered.

6.4 Galaxy N4

As in the unskewed case, there is a 3σ detection of an offset in galaxy N4. Interestingly there is no evidence for a skew in galaxy N4 from the shape of the posterior. This can be seen in Figures 25, where I have repeated the analysis used for galaxy N1, projecting

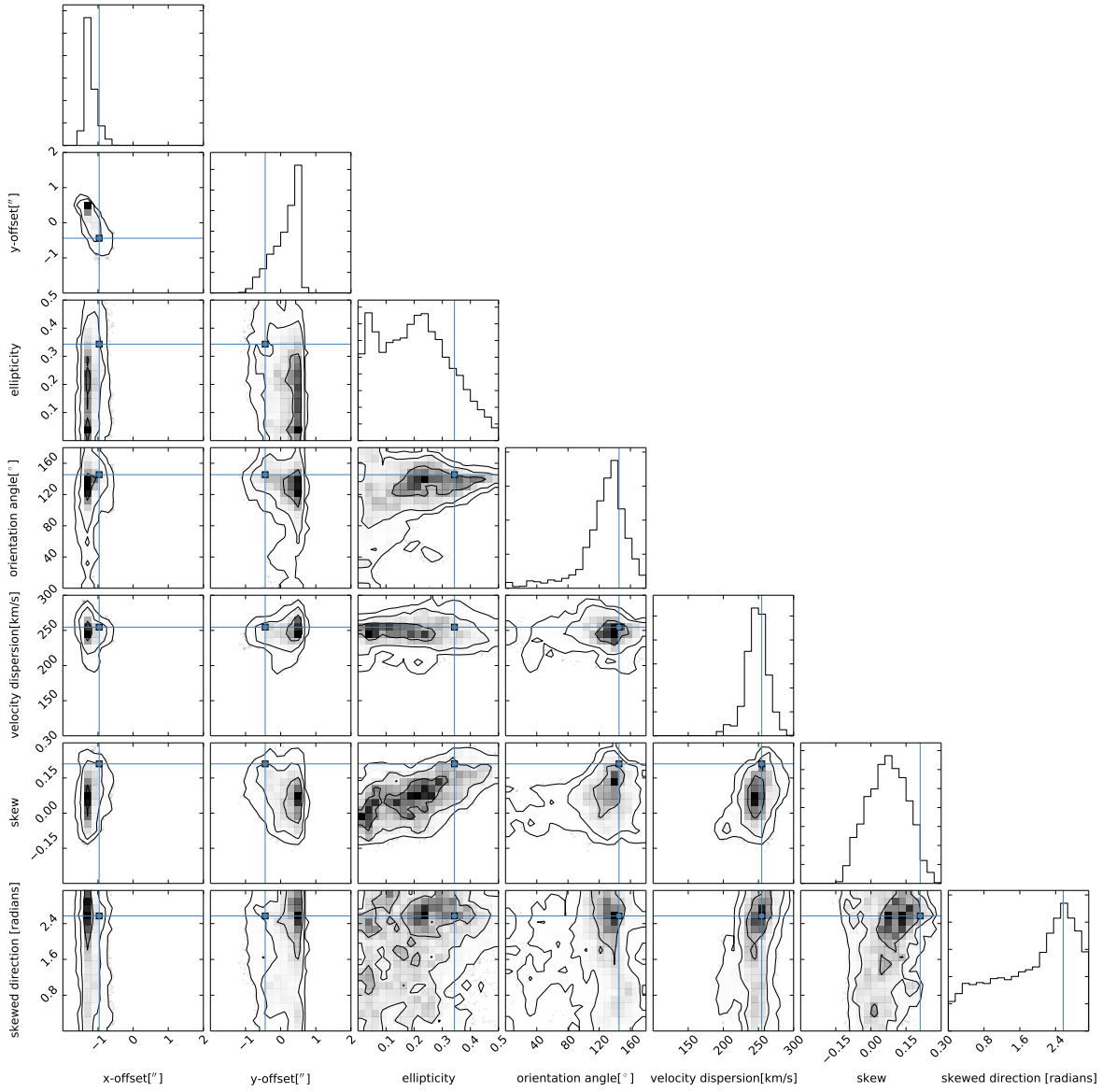

Figure 20: Posterior probability, from 10,000 samples, for parameters of galaxy N4, with contours showing the 1σ, 2σ and 3σ contour levels. The best fit model parameters are indicated in blue. The position has been rescaled so that $(x, y) = (0, 0)$ corresponds to the luminosity peak in galaxy N4. An offset is measured at the 3σ level. Small skews are preferred, although the best fit value is an outlier. The skew angle is defined anticlockwise from West.

the skew vector onto the offset vector, and a vector orthogonal to this.

The lack of any discernible suggestion of skew in galaxy N4 is challenging. If SIDM is really causing the offsets, why should there be a skew in one offset galaxy but not the other? There are many possible explanations. The first is that there actually is no skew present in galaxy N1, and large skews are favoured in the model due to some unknown systematics. Another possibility is that galaxy N4 lies in a higher density region, nearer the cluster core, so that the skew is less detectable. A third possibility is that MCMC cannot converge to the real skew in galaxy N4, since the angle of the offset is less well constrained than for galaxy N1. It is also possible, though unlikely, that treating all 4

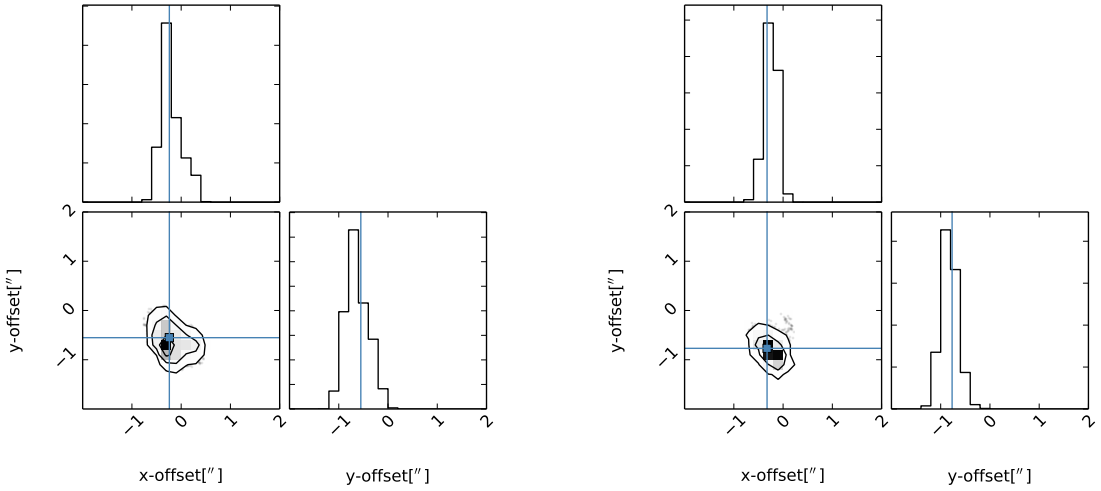

(a) Posterior of offsets in galaxy N1 with skew. (b) Posterior of offsets in galaxy N1 without skew.

Figure 21: The posterior, from 10,000 samples, of the offsets in galaxy N1 for the final models, with and without skew. The 1σ, 2σ and 3σ contours are shown. The best fit is shown in blue. The point (0,0) corresponds to the luminosity peak. The errors are slightly larger in the model with skew, but the offset is still just present at the 3σ level.

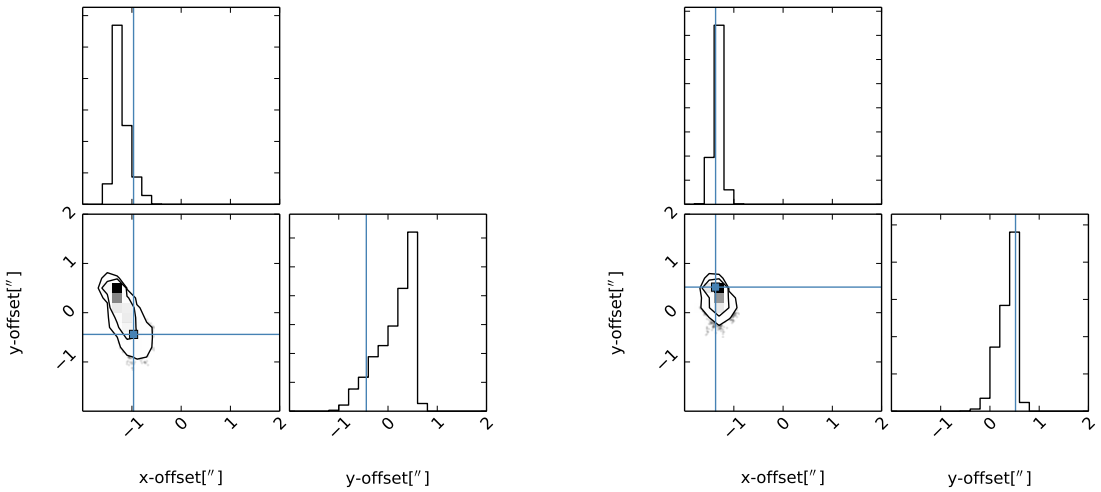

(a) Posterior of offsets in galaxy N4 with skew. (b) Posterior of offsets in galaxy N4 without skew.

Figure 22: The posterior, from 10,000 samples, of the offsets in galaxy N4 for the final models, with and without skew. The 1σ, 2σ and 3σ contours are shown. The best fit is shown in blue. The point (0,0) corresponds to the luminosity peak. The errors are slightly larger in the model with skew, but the offset is still present.

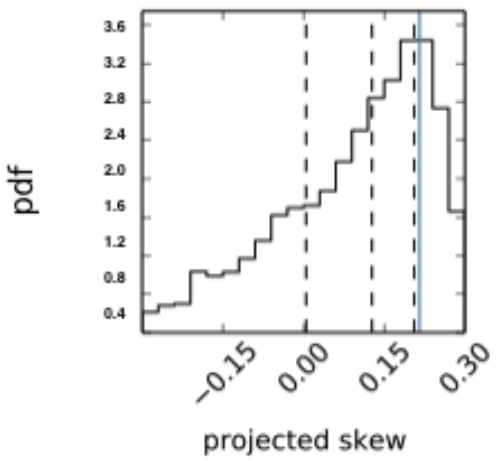

(a) Skew projection onto best fit offset vector.

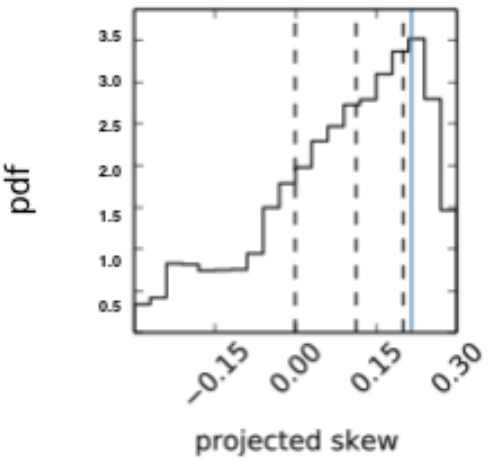

(b) skew projection at each step in MCMC.

Figure 23: The posterior of the skew vectors in galaxy N1 projected onto (a) the best fit offset vector and (b) the offset vector at each step in the MCMC. The Jacobian in transforming from a Polar to Cartesian space has been accounted for. The vertical dashed lines indicate the 25%, 50% and 75% quantiles. The blue line indicates the best fit value. There is little difference between the two projections.

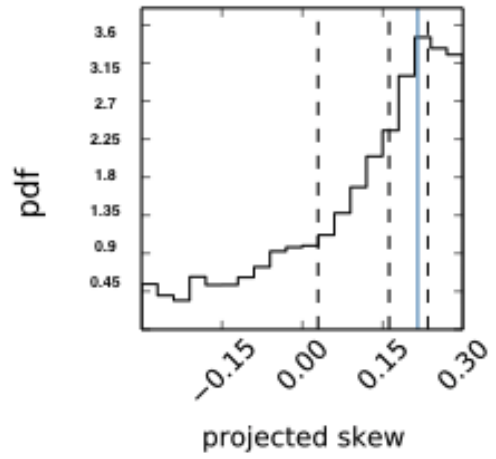

(a) skew projected onto best fit offset vector

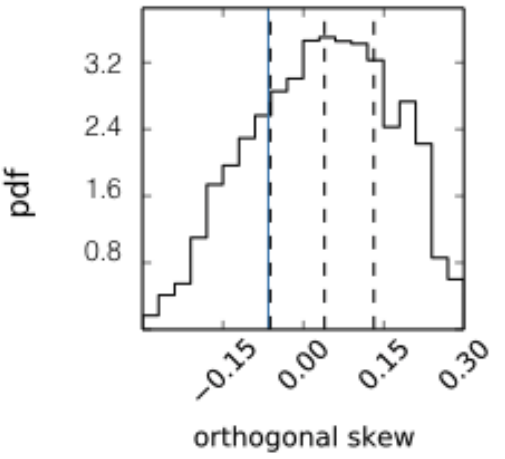

(b) skew projected orthogonally to offset

Figure 24: The posterior of the skew vectors in galaxy N1 projected onto (a) the best fit offset vector and (b) the direction orthogonal to this. The Jacobian has been accounted for and the priors have been adjusted as described in section 3.6. In the case of the orthogonal skew, I weight by $\frac{1}{.3^2-y^2}$ instead, as this is the correct weighting function for this projection. The vertical dashed lines indicate the 25%, 50% and 75% quantiles. The blue line indicates the best fit value. There is a preference for a skew that is consistent with SIDM, and no such preference is shown for a skew component that is orthogonal to the offset vector.

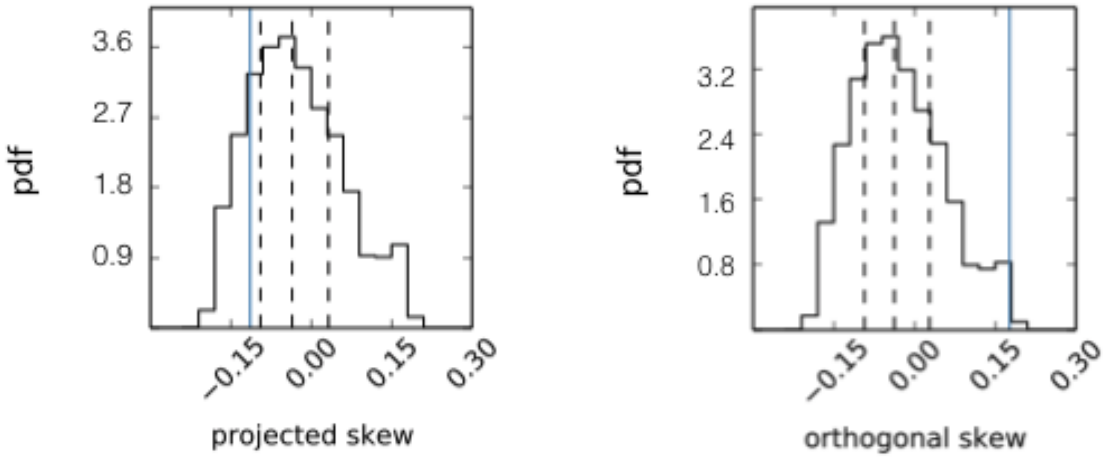

(a) skew projected onto best fit offset vector

(b) skew projected orthogonally to offset

Figure 25: The posterior of the skew vectors in galaxy N4 projected onto (a) the best fit offset vector and (b) the direction orthogonal to this. Everything else is the same as in Figure 24. The best fit skew, indicated in blue is clearly an outlier. Both posteriors peak near $s_{projected} = s_{orthogonal} = 0$, indicative of no skew.

galaxies as having the same redshift leads to the discrepancy. Galaxy N4 has a redshift of z=0.96 while the redshifts of galaxies N1, N2 and N3 are all z= 0.99 . See the appendix for a further discussion and an estimate of the importance of the redshift. We must keep in mind, however, that large skews, as seen in Figure 16, have not been ruled out, even though the posterior favours smaller skews.

6.5 Estimating the Cross-Section of DM

Since the skew does little to affect the offset positions, the new offset positions in galaxies N1 and N4 provide new constraints for the cross section of DM. To do this we will use equation (31). For the density, and infall velocity, I use the same estimates as [23], that is, I take $v = 1500$ km s^{-1} and $\rho = 4$ Gev cm^{-3}. In both cases, $r_{core} = 0.1828$ kpc. The remaining parameter estimates, from the fiducial model, are given in Table 5. I have taken care to rescale the velocity dispersion output from Lenstool using equation (41). The offset in galaxy N1 leads to a lower bound of $\frac{\tilde{\sigma}}{m_{DM}} \gtrsim 1.4$ cm^2 g^{-1}, while the offset in galaxy N4 lead to an estimate of $\frac{\tilde{\sigma}}{m_{DM}} \gtrsim 2.7$ cm^2 g^{-1}. As the offset in direction galaxy N4 suggests that galaxy N4 might have travelled through a higher density region in the past, we take:

$$\frac{\tilde{\sigma}}{m_{DM}} \gtrsim 1.4 \text{ cm}^2 \text{ g}^{-1}, \tag{56}$$

as our best estimate. It is worth noting that in equation (31) the cross-section is sensitively dependent on the infall velocity, going as $1/v^2$. Thus, an extremely large infall velocity could result in a further order of magnitude reduction in the cross-section.

Table 5: Parameter values used for cross-section calculation.

Galaxy	σ_{lt}^2 [km/s]	a_{stars} [kpc]	S [kpc]
N1	154.05	0.529	1.06
N4	254.59	1.37	1.94

7 Conclusion and Directions for Future Work

I have presented a new mass model for the galaxy cluster Abell 3827. Choosing flat priors for the position of *all* galaxies doubles the number of offset detections. Data from new VLT/MUSE observations tightens the constraints on the newly detected offset. These offsets suggest a lower bound on the cross-section of DM of $\tilde{\sigma}/m_{DM} \gtrsim 1.4$ cm g^{-1}. As discussed in this thesis, care is needed when comparing this to other estimates, as these may calculate the cross-section in a different way.

I have also developed a parametric lens model for skewed mass distributions, which can be used to search for DM tails in colliding galaxies. Although the skews in all galaxies are consistent with no skew, the converse is also true, that is, I could find no clear indication that the DM subhalos in A3827 had to be perfectly elliptical. Despite this, existing offset measurements are likely still valid, as it appears that skew does not significantly change the predicted position of the DM peak.

There are early signs that there may be a DM tail that is consistent with SIDM particles being scattered out of the potential well of galaxy N1. More work is needed to determine whether this is physical, or an artefact of systematics of parametric lens modelling. This is a question that likely cannot be answered in cluster lensing, as there are too many unknowns to isolate the effects of skewed galaxy scale DM halos on the lensing signal. Fortunately there is a path forward. Numerous field galaxy pairs have been identified in the SLACS survey, and an offset between dark and luminous matter has already been identified in one such pair [41]. In galaxies where luminous to dark matter offsets are present, the direction of the DM tail should serve a consistency check for the SIDM hypothesis. If this proves to be fruitful, then these systems should be simulated and the parametric halos presented in this thesis should be calibrated against different SIDM models in these simulations.

References

[1] Matthias Bartelmann and Peter Schneider. Weak gravitational lensing. *Physics Reports*, 340(4):291–472, 2001.

[2] MC Bento, O Bertolami, R Rosenfeld, and L Teodoro. Self-interacting dark matter and the higgs boson. *Physical Review D*, 62(4):041302, 2000.

[3] Kimberly K Boddy, Jonathan L Feng, Manoj Kaplinghat, and Tim MP Tait. Self-interacting dark matter from a non-abelian hidden sector. *Physical Review D*, 89(11):115017, 2014.

[4] RR Bourassa and R Kantowski. The theory of transparent gravitational lenses. *The Astrophysical Journal*, 195:13–21, 1975.

[5] JAMES BULLOCK. 3. notes on the missing satellites problem. *Local Group Cosmology*, 20:95, 2013.

[6] WL Burke. Multiple gravitational imaging by distributed masses. *The Astrophysical Journal*, 244:L1, 1981.

[7] Eric D Carlson, Marie E Machacek, and Lawrence J Hall. Self-interacting dark matter. *The Astrophysical Journal*, 398:43–52, 1992.

[8] Sean M Carroll. *Spacetime and geometry. An introduction to general relativity*, volume 1. 2004.

[9] WJG De Blok. The core-cusp problem. *Advances in Astronomy*, 2010, 2009.

[10] Giulia Despali, Carlo Giocoli, Mario Bonamigo, Marceau Limousin, and Giuseppe Tormen. A look to the inside of haloes: a characterisation of the halo shape as a function of overdensity in the planck cosmology. *arXiv preprint arXiv:1605.04319*, 2016.

[11] JM Diego, P Protopapas, HB Sandvik, and M Tegmark. Non-parametric inversion of strong lensing systems. *Monthly Notices of the Royal Astronomical Society*, 360(2):477–491, 2005.

[12] Daniel Foreman-Mackey. corner.py: Scatterplot matrices in python. *The Journal of Open Source Software*, 24, 2016.

[13] Carlo Giocoli, Massimo Meneghetti, Matthias Bartelmann, Lauro Moscardini, and Michele Boldrin. moka: a new tool for strong lensing studies. *Monthly Notices of the Royal Astronomical Society*, 421(4):3343–3355, 2012.

[14] David Harvey, Jean-Paul Kneib, and Mathilde Jauzac. Systematic or signal? how dark matter misalignments can bias strong lensing models of galaxy clusters. *Monthly Notices of the Royal Astronomical Society*, 458(1):660–665, 2016.

[15] David Harvey, Richard Massey, Thomas Kitching, Andy Taylor, and Eric Tittley. The nongravitational interactions of dark matter in colliding galaxy clusters. *Science*, 347(6229):1462–1465, 2015.

[16] David Harvey, Eric Tittley, Richard Massey, Thomas D Kitching, Andy Taylor, Simon R Pike, Scott T Kay, Erwin T Lau, and Daisuke Nagai. On the cross-section of dark matter using substructure infall into galaxy clusters. *Monthly Notices of the Royal Astronomical Society*, 441(1):404–416, 2014.

[17] Lars Hernquist. An analytical model for spherical galaxies and bulges. *The Astrophysical Journal*, 356:359–364, 1990.

[18] M Jauzac, D Eckert, J Schwinn, D Harvey, CM Baugh, A Robertson, S Bose, R Massey, M Owers, H Ebeling, et al. The extraordinary amount of substructure in the hubble frontier fields cluster abell 2744. *arXiv preprint arXiv:1606.04527*, 2016.

[19] R Joseph, F Courbin, and J-L Starck. Multi-band morpho-spectral component analysis deblending tool (muscadet): Deblending colourful objects. *Astronomy & Astrophysics*, 589:A2, 2016.

[20] Eric Jullo, Jean-Paul Kneib, Marceau Limousin, Ardis Eliasdottir, PJ Marshall, and Tomas Verdugo. A bayesian approach to strong lensing modelling of galaxy clusters. *New Journal of Physics*, 9(12):447, 2007.

[21] Eric Jullo, Priyamvada Natarajan, Jean-Paul Kneib, Anson D'Aloisio, Marceau Limousin, Johan Richard, and Carlo Schimd. Cosmological constraints from strong gravitational lensing in clusters of galaxies. *Science*, 329(5994):924–927, 2010.

[22] Felix Kahlhoefer, Kai Schmidt-Hoberg, Mads T Frandsen, and Subir Sarkar. Colliding clusters and dark matter self-interactions. *Monthly Notices of the Royal Astronomical Society*, 437(3):2865–2881, 2014.

[23] Felix Kahlhoefer, Kai Schmidt-Hoberg, Janis Kummer, and Subir Sarkar. On the interpretation of dark matter self-interactions in abell 3827. *Monthly Notices of the Royal Astronomical Society: Letters*, 452(1):L54–L58, 2015.

[24] Nick Kaiser and Gordon Squires. Mapping the dark matter with weak gravitational lensing. *The Astrophysical Journal*, 404:441–450, 1993.

[25] Manoj Kaplinghat, Sean Tulin, and Hai-Bo Yu. Self-interacting dark matter benchmarks. *arXiv preprint arXiv:1308.0618*, 2013.

[26] Aggeliki Kassiola and Israel Kovner. Elliptic mass distributions versus elliptic potentials in gravitational lenses. *The Astrophysical Journal*, 417:450, 1993.

[27] Stacy Y Kim, Annika HG Peter, and David Wittman. In the wake of dark giants: New signatures of dark matter self interactions in equal mass mergers of galaxy clusters. *arXiv preprint arXiv:1608.08630*, 2016.

[28] Jean-Paul Kneib and Priyamvada Natarajan. Cluster lenses. *The Astronomy and Astrophysics Review*, 19(1):1–100, 2011.

[29] Alexander Kusenko and Paul J Steinhardt. Q-ball candidates for self-interacting dark matter. *Physical review letters*, 87(14):141301, 2001.

[30] Jori Liesenborgs, Sven De Rijcke, and Herwig Dejonghe. A genetic algorithm for the non-parametric inversion of strong lensing systems. *Monthly Notices of the Royal Astronomical Society*, 367(3):1209–1216, 2006.

[31] M Limousin, JP Kneib, Sebastien Bardeau, P Natarajan, O Czoske, I Smail, H Ebeling, and GP Smith. Truncation of galaxy dark matter halos in high density environments. *Astronomy & Astrophysics*, 461(3):881–891, 2007.

[32] Marceau Limousin, Jean-Paul Kneib, and Priyamvada Natarajan. Constraining the mass distribution of galaxies using galaxy-galaxy lensing in clusters and in the field. *Monthly Notices of the Royal Astronomical Society*, 356(1):309–322, 2005.

[33] Maxim Markevitch, AH Gonzalez, D Clowe, A Vikhlinin, W Forman, C Jones, S Murray, and W Tucker. Direct constraints on the dark matter self-interaction cross section from the merging galaxy cluster 1e 0657? 56. *The Astrophysical Journal*, 606(2):819, 2004.

[34] Richard Massey, Liliya Williams, Renske Smit, Mark Swinbank, Thomas D Kitching, David Harvey, Mathilde Jauzac, Holger Israel, Douglas Clowe, Alastair Edge, et al. The behaviour of dark matter associated with four bright cluster galaxies in the 10 kpc core of abell 3827. *Monthly Notices of the Royal Astronomical Society*, 449(4):3393–3406, 2015.

[35] M Meneghetti, P Natarajan, D Coe, E Contini, G De Lucia, C Giocoli, A Acebron, S Borgani, M Bradac, JM Diego, et al. The frontier fields lens modeling comparison project. *arXiv preprint arXiv:1606.04548*, 2016.

[36] Chien Y Peng, Luis C Ho, Chris D Impey, and Hans-Walter Rix. Detailed decomposition of galaxy images. ii. beyond axisymmetric models. *The Astronomical Journal*, 139(6):2097, 2010.

[37] Andrew Pontzen and Fabio Governato. How supernova feedback turns dark matter cusps into cores. *Monthly Notices of the Royal Astronomical Society*, 421(4):3464–3471, 2012.

[38] Andrew Robertson, Richard Massey, and Vincent Eke. What does the bullet cluster tell us about self-interacting dark matter? *arXiv preprint arXiv:1605.04307*, 2016.

[39] Till Sawala, Carlos S Frenk, Azadeh Fattahi, Julio F Navarro, Richard G Bower, Robert A Crain, Claudio Dalla Vecchia, Michelle Furlong, John Helly, Adrian Jenkins, et al. Local group galaxies emerge from the dark. *arXiv preprint arXiv:1412.2748*, 2014.

[40] Matthieu Schaller, Andrew Robertson, Richard Massey, Richard G Bower, and Vincent R Eke. The offsets between galaxies and their dark matter in λ cold dark matter. *Monthly Notices of the Royal Astronomical Society: Letters*, 453(1):L65–L69, 2015.

[41] Yiping Shu, Adam S Bolton, Leonidas A Moustakas, Daniel Stern, Arjun Dey, Joel R Brownstein, Scott Burles, and Hyron Spinrad. Kiloparsec mass/light offsets in the galaxy pair-lyman alpha emitter lens system sdss j1011+ 0143. *The Astrophysical Journal*, 820(1):43, 2016.

[42] David N Spergel and Paul J Steinhardt. Observational evidence for self-interacting cold dark matter. *Physical Review Letters*, 84(17):3760, 2000.

[43] Jie Wang, Carlos S Frenk, Julio F Navarro, Liang Gao, and Till Sawala. The missing massive satellites of the milky way. *Monthly Notices of the Royal Astronomical Society*, 424(4):2715–2721, 2012.

[44] Liliya LR Williams and Prasenjit Saha. Light/mass offsets in the lensing cluster abell 3827: evidence for collisional dark matter? *Monthly Notices of the Royal Astronomical Society*, 415(1):448–460, 2011.

8 Appendix

8.1 A Note About Gravitational Lensing Assumptions

While modelling A3827, three assumptions about gravitational lensing have been made. Firstly, we have treated all the galaxies as lying at the same redshift, made the Thin Lens Approximation, and assumed that all lenses are static.

To see that these assumptions are valid, we will compare the Einstein Radius with and without these assumptions in idealised circumstances that actually overestimate the effects of making these assumptions. This radius will serve as a typical error length scale. In all cases this is smaller than the angular resolution of HST, which is $\sim 0.1''$, so the errors associated with these approximations can safely be ignored. In all cases the background source is assumed to lie at a redshift of $z = 1.24$, as in Abell 3827.

The first of these assumptions is relevant since in [34] the redshift of galaxies N1-N3 were measured at $z = 0.099$, while the redshift of galaxy N4 was measured at $z = 0.096$. However, to make the calculation easier for Lenstool, all galaxies are given a redshift of $z = 0.099$.

Let us approximate the mass of galaxy N4 with a point mass of $1.83 \times 10^{11} M_{\odot}$ which is consistent with the mass measured within $1.5''$ of the centre of galaxy N4 in [34]. The corresponding Einstein Radii for redshifts of $z = 0.096$ and $z = 0.099$ are $1.91''$ and $1.89''$ respectively. The difference is smaller than the angular resolution of HST, so it is safe to model all galaxies at the same redshift.

The Thin Lens Approximation is valid for a similar reason. If we approximate the mass of the entire central region of the cluster with a point mass of $3.5 \times 10^{12} M_{\odot}$, which is consistent with the mass measured in the central $8.33''$ in [34], and consider this lens at redshifts of $z = 0.1$ and $z = 0.099$ which differ by massive 3.37 Mpc i.e, about three times a cluster's typical cut radius, then the corresponding Einstein Radii are $8.17''$ and $8.21''$ respectively. Again, the difference is an order of magnitude smaller than the angular resolution of HST, and if we can move such large amounts of mass along the line-of-sight by such large distances, with such little effect, then the Thin Lens Approximation is clearly valid.

The final assumption made is that the lenses are static. This is too hard to check properly as we would have to solve the Einstein Equations to find how space is distorted for a moving point mass, and then solve the Geodesic Equation to find the deflection angle. However we can still provide a rough estimate of how important lens motion is by ignoring the effects of a dynamical space time and just imagine moving the lens instantaneously instead.

Recall that the deflection angle

$$\alpha = \text{constant} \times \int_{-\infty}^{\infty} \frac{\mathrm{d}x}{(1+x^2)^{3/2}}, \tag{57}$$

where we have put the impact parameter $b = 1$ to define a typical length scale. Now define

$$\begin{aligned} f(L) \equiv & \int_{-L}^{L} \frac{\mathrm{d}x}{(1+x^2)^{3/2}} \\ = & \frac{2L}{\sqrt{1+L^2}}, \end{aligned} \tag{58}$$

so that $f(\infty)$ gives the deflection angle up to multiplication of a constant. A plot of $f(L)$ is shown in Figure 26 in units of the impact parameter. It is clear that almost all the deflection occurs within 10 impact parameter lengths of the lens. However as a typical velocity is ~ 300km/s, which is ~ 1000 times slower than the speed of light, the lens will have barely moved while the photon is in a region that can be influenced by the lens. Thus it is safe to ignore the effects of a moving lens.

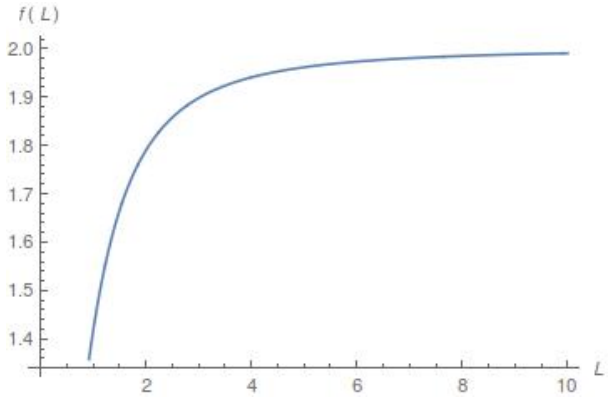

Figure 26: This shows how much of the deflection is caused within a distance L from the lens in units of the impact parameter. A value of 2 corresponds to the full deflection caused by the lens. This reminds us that light is deflected by twice the amount expected by Newtonian Theory.

8.2 Weighting Functions

Another way to introduce skew is to apply a weighting function $w(\mathbf{r}; \{a_i\})$ to the potential so that:

$$\psi(\mathbf{r}) \rightarrow \psi'(\mathbf{r}) \equiv w(\mathbf{r}; \{a_i\})\psi(\mathbf{r}), \tag{59}$$

where $\{a_i\}$ are a set of parameters. The deflection and surface mass density can then be computed by using the chain rule to find the first and second derivatives.

We consider perturbation weighting functions of the form:

$$w(\mathbf{r}; \{a_i\}) = 1 + sf(r, \theta) \tag{60}$$

where s is a skew parameter and, $f(r, \theta)$, written in polar coordinates, are considered. The second term acts as a perturbation away from elliptical symmetry of $O(s)$, with $s = 0$ corresponding to the elliptically symmetric case. We chose $f(r, \theta)$ to meet the following criteria:

- To ensure that the space about $s = 0$ is explored symmetrically in Lenstool, so that a non-zero skew is not artificially recovered, we restricted our attention to functions that satisfy:
$$sf(r, \theta) = -sf(r, \theta + \pi). \tag{61}$$
- We take $f(r, \theta)$ to be an increasing function of r. We found that this is necessary to avoid difficulties near the origin. However, this choice was initially physically motivated as it is hard to scatter particles from the centre of the potential well at $r = 0$.
- We take $f(r, \theta)$ to be bounded. This ensures that the surface mass density becomes negative only for extremely large r, well outside the region of interest.

Meeting these requirements, we take the weighting function as:

$$w(\mathbf{r}; s, \beta, \phi) = 1 + s \tan^{-1}\left(\beta \frac{r}{r_s}\right) \cos(\theta - \phi), \tag{62}$$

where r_s is a scale radius that non-dimensionalises the weighting function, β sets the radial dependence of the skew, and ϕ is the skew angle. Note that the inverse tangent form of the radial dependence is not physically motivated and other functional forms may work better as long as they meet the criteria given above.

It is important to stress that this weighting function is general and can be applied to any elliptical potential.

8.3 Pseudo Isothermal Skewed Potential with Weighting Function

By applying the weighting function given in equation 62 to the PIEMD potential, we create what will be referred to as the Weighted Pseudo Isothermal Skewed Potential (wPISP). This has been implemented in Lenstool, and will soon be publicly available as potential 812. The resulting surface mass densities of the new potentials are shown in Figure 27 and Figure 28.

The skewed distributions in Figure 27 are fairly well behaved, and, inside this 20 kpc, behave as intended. However the contours in Figure 27, where a larger radial dependence parameter has been taken, are not well behaved. The skew angle may no longer give the

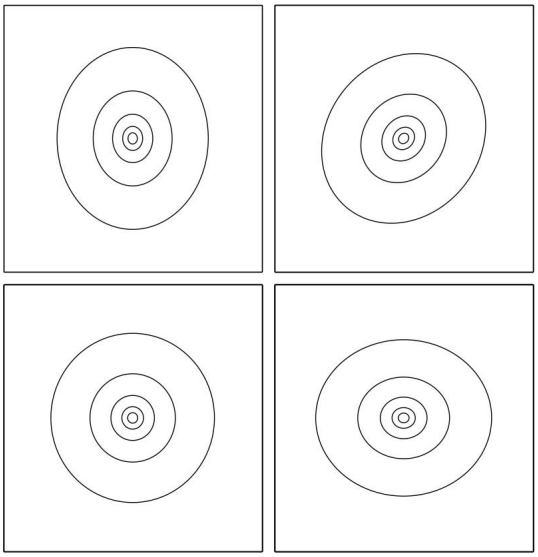

(a) PIEMD in 20×20 kpc box.

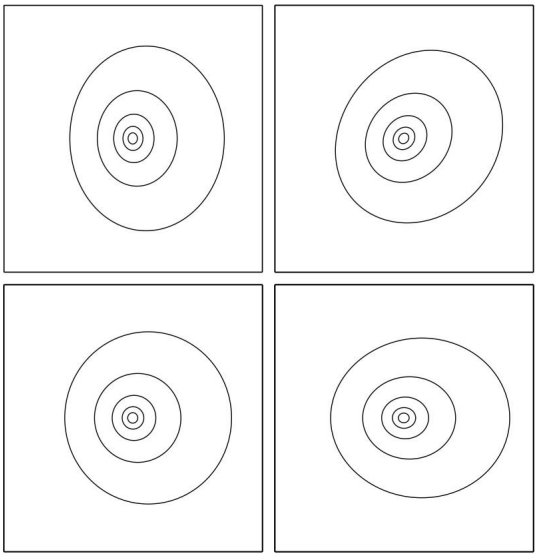

(b) wPISP with skew acting to the right

Figure 27: The left hand side shows four wPISP isodensity contours and the left hand side shows these same density profiles with skew. In all cases the cut radius is fixed to 73.1 kpc, the core radius is fixed to 0.183 kpc and the velocity dispersion is 180 km s^{-1}. The ellipticity is 0.15 for the three galaxies starting at the top left and going clockwise with orientations of 90°, 45° and 0° respectively, and where the galaxy in the bottom left has an ellipticity of 0. When the skew is applied, the scale radius r_s, is fixed to the core radius, the skew parameter $s = 0.3$ and the radial dependence parameter $\beta = 0.01$. Contours are logarithmically spaced by a factor of 2.

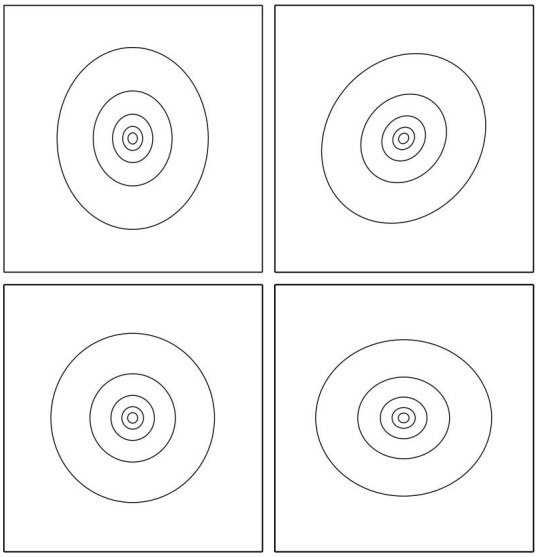

(a) PIEMD in 20×20 kpc box.

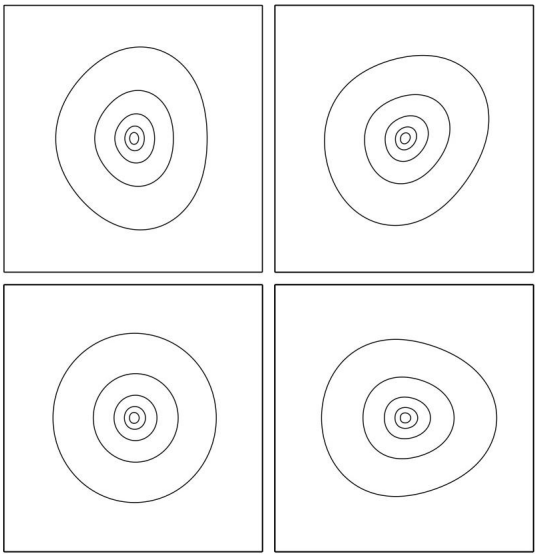

(b) wPISP with large β and skewed to the right.

Figure 28: Same as Figure 27, but with a larger radial dependence parameter of $\beta = 2$. When the skew is present, for large β values, the contour shapes become self-similar but isocentric at different radii, the direction of the skew reverses when it is acting in a direction orthogonal to the major axis. This sign reversal makes it difficult to draw physical conclusions from potentials with a large radial dependence parameter.

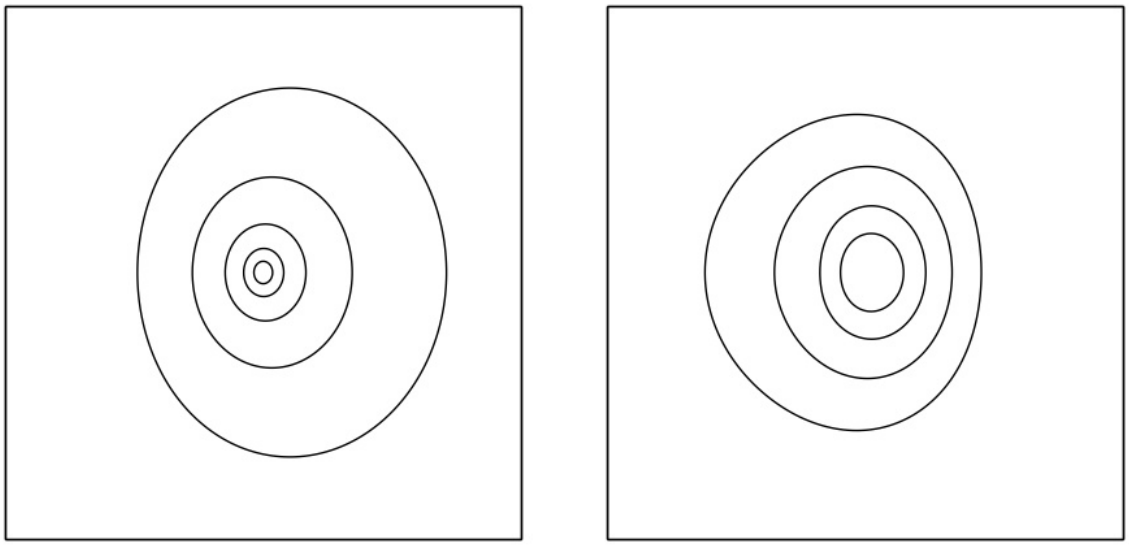

(a) PIEMD in 20×20 kpc box. (b) The same PIEMD in 200×200 kpc box.

Figure 29: This figure shows the effect of the transition region at large radii. The figures on the left and the right are the same WSPIEMD profiles at two different zooms. All parameters are the same as Figure 27.

direction of the skew depending on the orientation of the major axis. This behaviour is not actually restricted just to wPISPs with large radial dependence parameters. As shown in Figure 29, at sufficiently large radii, any wPISP that I have tested transitions to this unwanted behaviour. The reason this occurs, is that to avoid negative mass densities, the weight function was chosen so that the size of the perturbation away from ellipticial symmetry does not grow indefinitely with radius. A poorly behaved transition region is the compromise that has been made to avoid negative surface mass densities. This aphysical behaviour is not a problem as long as s and β are chosen so that this transition region is forced to a large enough radius to not affect the strong lensing region. It is extremely important when modelling with a wPISP to identify which region of the (s, β)-parameter space should be explored.

In general, smaller values of β push the transition region to larger radii. However, smaller values of β also increases the radius at which skew becomes important. This is far from ideal when modelling Abell 3827, as it greatly restricts how large the skew can be made at small radii while still ensuring that the transition occurs outside the strong lensing region. In general, the larger the value of β, the smaller the range of s can be to ensure that the transition region occurs sufficiently far away from the strong lensing region. I have also found that smaller values for the cut radius, and larger values for the ellipticity reduces the size of the transition region radius.

It can be seen that the position of the peak will change relative to where it would have been if there was no skew. We will refer to the peak of the wPISP as the *true peak* and where the peak would lie if there was no skew present as the *reference point.*

To compute the total mass of a wPISP, first note the mass of a PIEMD, M_{PIEMD}, is given by:

$$M_{\text{PIEMD}} = \frac{\pi \sigma_0^2 r_{\text{cut}}}{G} \left(1 - \epsilon^2\right). \tag{63}$$

as given in [32], with an additional factor of $1 - \epsilon^2$ to account for the ellipticity which

enters into the Jacobian when integrating. This formula is derived by finding the mass inside an ellipse with elliptical radius r_{em} and then taking the limit as $r_{em} \to \infty$. For the case of a wPISP, we integrate over a circular region centred on the reference point $\mid r \mid < R$ instead. This allows us to integrate out the θ-dependence and find that the mass inside this radius for a PIEMD and wPISP are the same that is:

$$\frac{c^2}{8\pi G}\frac{D_s}{D_l D_{ls}}\int_{|\mathbf{r}|<R}\nabla^2\psi \ \mathrm{d}A = \frac{c^2}{8\pi G}\frac{D_s}{D_l D_{ls}}\int_{|\mathbf{r}|<R}\nabla^2\left(w\psi\right) \ \mathrm{d}A. \tag{64}$$

Then taking the limit as $\mid \mathbf{r} \mid \to \infty$ and noting that the left hand side will converge to the total mass of a PIEMD with ellipticity ϵ implies

$$M_{\mathrm{wPISP}} = M_{\mathrm{PIEMD}}. \tag{65}$$

Another way of saying this is, that for a general weighting function $w(\mathbf{r};\{a_i\})$, there exists a weighting amplitude $A(\{a_i\})$, that normalises the density, such that, the total mass remains unchanged, and that, for the weighting function we have chosen, $A(s,\beta,\phi) = 1$ for all allowed $\{s,\beta,\phi\}$.

To insure that the new potential does not falsely predict skew I tested it on the *Example with Images* simulation available in Lenstool. In this simulation 3 background sources are lensed into two images each by a PIEMD. I gave the skew parameter a flat prior, $s \in [0.3, 0.3]$ with $\beta = 0.01$. This recovered a best fit value of $s = 0.002^{+0.002}_{-0.002}$. For comparison, when I gave some of the galaxies in Abell 3827 the same parameters I found that the best fit skew value could be as large as $O(0.1)$.

8.4 Pseudo Isothermal Varying Ellipticity Mass Distribution (PIVEMD)

Simulations performed in [10] predict that the ellipticity of a cluster scale halo changes as a function of radius becoming more elongated further from the centre. As an additional application of the weighting function formalism, a parametric mass density with an ellipticity that varies as a function of radius is introduced. The idea is to take a weighted sum of two different mass densities with different ellipticities. This has been done by applying the weighting function directly to the mass density, as applying the weighting function to the potential does not work in this case. To make this work in an MCMC setting, the deflection angles must be computed once, using numerical integration, and put into a look up table to speed up computation.

To construct such a mass density, it is chosen to have the following form:

$$\rho\left(\mathbf{r}\right) = \rho_{\epsilon_1}\left(\mathbf{r}\right) w_1\left(\mathbf{r}\right) + \rho_{\epsilon_2}\left(\mathbf{r}\right) w_2\left(\mathbf{r}\right) \tag{66}$$

where $\rho_{\epsilon_1}\left(\mathbf{r}\right)$ and $\rho_{\epsilon_2}\left(\mathbf{r}\right)$ are two elliptical profiles with ellipticity ϵ_1 and ϵ_2 respectively with all the other parameters for these two densities shared.

The weighting functions w_i are chosen to meet the following criteria:

- One ellipticity dominates at small r and the other ellipticity dominates as large r. To do this we let $w_1\left(\mathbf{r}\right) \to 1$ as $r \to \infty$, $w_1\left(\mathbf{r}\right) \to 0$ as $r \to 0$, $w_2\left(\mathbf{r}\right) \to 0$ as $r \to \infty$ and $w_2\left(\mathbf{r}\right) \to 1$ as $r \to 0$.

- To normalise the total mass I take: $w_1\left(\mathbf{r}\right) + w_2\left(\mathbf{r}\right) = 1$ for all r.

Although this is quite a general set of conditions we take, for example:

$$\begin{aligned} w_1(\mathbf{r}) &= 1 - e^{-\beta r} \\ w_2(\mathbf{r}) &= e^{-\beta r}, \end{aligned} \tag{67}$$

where β controls the radial dependence. The resulting mass distribution for this weighted sum is given in Figure 30.

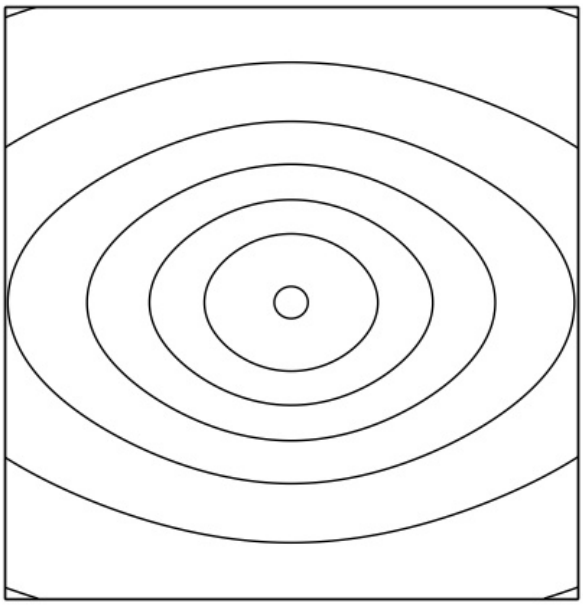

Figure 30: Isodensity contours for a radially varying weighted sum of two PIEMDs with different ellipticities.

8.5 Mass Models of Abell 3827 Using wPISPs

I tried to model Abell 3827 using the wPISP for the four central ellipticals. I encountered many problems. Firstly, the computation is extremely slow as Lenstool has to compute the lensing potential ψ. This is much slower than computing the first derivatives only, which is the case for the PIEMD and the PISP.

The main problem, however, is caused by the transition region. In order to ensure the transition region lies sufficiently outside the Einstein Radius, the skew parameter s must be restricted to very small values. This can be mitigated somewhat by choosing a smaller radial dependence parameter β. However, in all cases, it is impossible to get very much skew near the centre of the lens while still ensuring that the transition region lies well outside the strong lensing region. As a result, for wPISP models, the skew angle could not be constrained to within 180°, making it impossible to draw physical conclusions.

It is possible that this potential could be used to detect skew in systems with smaller Einstein Radii, so that the skew parameter, s, is allowed to vary over a larger range. In particular, isolated field galaxy pairs identified in the SLACS survey could prove an exciting testing ground for this new potential. Although, the PISP works better in the setting of Abell 3827, the ability to vary the radius at which skew becomes important is still an advantage of the weighting function approach over the coordinate transformation one.

8.6 Alternative Models and Robustness Checks of the Mass Modelling in Abell 3827

I have run a few other models in Lenstool to test the effects of fixing the ellipticity, varying the stellar mass, and varying the cut radius.

The ellipticity is badly constrained. This can be seen in Figure 17. For this reason I have constructed two additional models where I have fixed the ellipticity and orientation angle for each galaxy to the stellar parameters as found in Galfit. In the first model I fixed the skew to $s = 0$, while in the second I allowed the galaxies to have a free skew. Fixing the ellipticity is problematic from the outset, as the ellipticity of galaxy N4 is likely wrong, as it is significantly larger than for the other galaxies, probably due to the stellar light contamination from the nearby Milky Way Star, along the line-of-sight. The reduced χ^2 for the model with fixed ellipticity and fixed skew is 1.86, in comparison to 1.88 for the model with free ellipticity and fixed skew. This is not a statistically significant improvement. Nevertheless the offset measurements in galaxies N1 and N4 are consistent in both models. When the skew parameter is allowed to vary, the skew in galaxy N1, is consistent between the models with fixed and free ellipticities.

I also considered varying the cut radius in galaxies N1-N4, as it is normally possible to constrain this parameter for galaxy scale halos. I allowed the cut radius to vary between $5''$ and $50''$. I found that the cut radius could only be constrained to within $\sim 15''$ (~ 30 kpc) and that the inclusion of this parameter did not improve the χ^2. For this reason I fixed the cut radius in the final analysis.

Finally, as a robustness check, I tested the effects of increasing and decreasing the stellar mass associated with offset galaxies N1 and N4 by 50%. This was done by manually adjusting the velocity dispersion. In both cases the offsets and skews for galaxies N1 were unaffected. This was expected as the stellar mass only contributes a small fraction to the total mass of the cluster.

8.7 Position of Multiple Images

Table 6: Position of multiple images and their assigned errors in the fiducial lens model.

Name	RA	DEC	Error [″]
Ao.1	330.47479	−59.943580	0.2
Ao.2	330.46649	−59.946650	0.2
Ao.3	330.46828	−59.944112	0.2
Ao.4	330.47407	−59.946239	0.2
Aa.1	330.47559	−59.944009	0.2
Aa.2	330.46725	−59.947321	0.2
Aa.3	330.46871	−59.944215	0.2
Aa.4	330.47489	−59.946312	0.2
Aa.5	330.47529	−59.946349	0.2
Aa.6	330.47546	−59.946523	0.2
Aa.7	330.47047	−59.945183	0.2
Aa.8	330.47079	−59.946112	0.8
Ab.1	330.47571	−59.943954	0.2
Ab.2	330.46741	−59.947260	0.2
Ab.3	330.46852	−59.944283	0.2
Ab.4	330.47515	−59.946584	0.2
Ac.1	330.47489	−59.943958	0.2
Ac.2	330.46669	−59.947267	0.2
Ac.3	330.46912	−59.943994	0.2
Ac.4	330.47441	−59.946030	0.2
Ad.1	330.47537	−59.943594	0.2
Ad.2	330.46685	−59.946564	0.2
Ad.3	330.46784	−59.944468	0.2
Ad.4	330.47326	−59.947020	0.2
Ae.1	330.47345	−59.943276	0.2
Ae.2	330.46590	−59.946186	0.2
Ae.3	330.46837	−59.943805	0.2
Ae.4	330.47315	−59.946447	0.2
Af.1	330.47417	−59.943267	0.2
Af.2	330.46621	−59.945961	0.2
Af.3	330.46745	−59.944289	0.2
Af.4	330.47249	−59.946730	0.2